

Contents lists available at [ScienceDirect](https://www.sciencedirect.com)

Remote Sensing of Environment

journal homepage: www.elsevier.com/locate/rse

Ocean color algorithms to estimate the concentration of particulate organic carbon in surface waters of the global ocean in support of a long-term data record from multiple satellite missions

Dariusz Stramski^{*}, Ishan Joshi, Rick A. Reynolds

Marine Physical Laboratory, Scripps Institution of Oceanography, University of California San Diego, La Jolla, CA 92093-0238, USA

ARTICLE INFO

Keywords:

Satellite remote sensing
Ocean color
Bio-optical algorithms
Particulate organic carbon
Ocean optics

ABSTRACT

As the concentration of particulate organic carbon (POC) in the surface ocean plays a key role in marine biogeochemical cycles and ecosystems, its assessment from satellite observations of the global ocean is of significant interest. To achieve a global multi-decadal data record of POC by merging observations from multiple satellite ocean color missions, we formulated a new suite of empirical POC algorithms for several satellite sensors. For the algorithm development we assembled a field dataset of concurrent POC and remote-sensing reflectance, $R_{rs}(\lambda)$, measurements collected in all major ocean basins encompassing tropical, subtropical, and temperate latitudes as well as the northern and southern polar latitudes. This dataset is characterized by a globally-representative probability distribution of POC with a broad range of values between about 10 and 1000 mg m^{-3} . This development dataset was created with the use of additional inclusion and exclusion criteria based on well-assured and documented consistency of measurement protocols as well as specific bio-optical and particle characteristics of seawater which are consistent with vast areas of open-ocean pelagic environments.

To formulate the algorithms the development dataset was subject to parametric regression analysis. Overall we evaluated over seventy formulas for estimating POC from $R_{rs}(\lambda)$ using seven distinctly different algorithmic categories, each with a fundamentally different definition of independent variable involving $R_{rs}(\lambda)$. Through the goodness-of-fit analysis, we selected the best candidate POC algorithms, referred to as the hybrid algorithms, which are tuned specifically for the spectral bands of SeaWiFS, MODIS, VIIRS, MERIS, and OLCI satellite sensors. These hybrid algorithms consist of two components, the MBR (Maximum Band Ratio)-OC4 cubic polynomial function and BRDI (Band Ratio Difference Index) quintic polynomial function. The MBR-OC4 uses four spectral bands and the BRDI three spectral bands from the blue-green spectral region. The MBR-OC4 algorithm is used for $\text{POC} > 25 \text{ mg m}^{-3}$ and the BRDI for $\text{POC} < 15 \text{ mg m}^{-3}$. In the transition region the weighting approach is applied to POC derived from the two algorithmic formulas. While the main role of the BRDI is to improve POC estimates in ultraoligotrophic waters where POC is very low, the MBR-OC4 provides improvements, compared with the predecessor algorithms, over a broader range of POC but especially for relatively high POC values. A preliminary analysis of field-satellite matchup datasets based on SeaWiFS and MODIS-Aqua observations shows improved performance of hybrid algorithms compared with current standard algorithms for both SeaWiFS and MODIS. In addition, a reasonable consistency is demonstrated between POC derived from hybrid algorithms applied to example satellite observations with SeaWiFS, MODIS-Aqua, and VIIRS-SNPP. The suite of newly developed algorithms provides the potential next generation version of global algorithms that better represents the spatial and temporal variability within a broader range of POC than the predecessor global algorithms, while also offering a capability to generate a long-term sensor-to-sensor consistent data record of POC that begins with the launch of SeaWiFS mission in 1997.

^{*} Corresponding author.

E-mail address: dstramski@ucsd.edu (D. Stramski).

<https://doi.org/10.1016/j.rse.2021.112776>

Received 24 April 2021; Received in revised form 19 October 2021; Accepted 25 October 2021

0034-4257/© 2021 The Authors. Published by Elsevier Inc. This is an open access article under the CC BY-NC-ND license

(<http://creativecommons.org/licenses/by-nc-nd/4.0/>).

1. Introduction

The standing stock of particulate organic carbon (POC) in the upper sunlit layer of the ocean is linked to marine biogeochemical processes and ecosystem characteristics, such as carbon export from the surface to the deep ocean and the availability of food for marine biota. Whereas the particulate organic matter in the surface ocean is generated largely by photosynthesis in phytoplankton cells, other types of planktonic organisms such as bacteria and zooplankton as well as non-living organic particles also contribute to POC. Although the POC stock is small compared to dissolved carbon pools in the ocean, the POC constituents have relatively short turnover times and are responsible for relatively large carbon fluxes. Numerous biological and chemical transformations and physical transport and mixing processes produce significant variations in POC on different temporal and spatial scales. For example, the particulate organic matter can be partially exported from the surface ocean into the deeper layers of the ocean via the “biological pump”, transferred to higher trophic levels within the food web, and transformed into dissolved organic carbon (DOC) and dissolved inorganic carbon (DIC) pools (e.g., Eppley and Peterson, 1979; Fenchel, 1988; Volk and Hoffert, 1985; Volkman and Tanoue, 2002; Wakeham and Lee, 1993). Local variations in POC can be also caused by transport of particulate matter from distant locations, including transport of terrestrially-derived particulate matter (e.g., Bianchi et al., 1997; Lovecchio et al., 2017).

Satellite-derived data record of POC in the surface ocean provides a means to quantify the magnitude and potential presence of multi-year trends in POC stock on global and basin scales in support of ocean biogeochemistry and ecosystem studies (e.g., Allison et al., 2010a; Duforêt-Gaurier et al., 2010; Gardner et al., 2006; Loisel et al., 2002; Stramska, 2009; Stramska and Cieszyńska, 2015). Monitoring the rates of change in POC in the upper ocean using satellite observations provides a means for advancing a methodology to diagnose the POC fluxes, such as primary production, export to the deep ocean and transformations to DOC and DIC pools, and constrain the uncertainties of carbon budget (Allison et al., 2010a). The total POC pool in the upper ocean also provides essential information and constraints for the estimation of phytoplankton carbon biomass and carbon-based primary production from satellite observations (e.g., Behrenfeld et al., 2005; Behrenfeld et al., 2013; Evers-King et al., 2017; Kostadinov et al., 2016). The assimilation of satellite-derived POC products into global coupled models of physical, biogeochemical and radiative processes provides an added value in the quest for better understanding and quantifying the effects and fate of carbon entering the oceans from the atmosphere, and potential responses and feedbacks of ocean ecosystems to climate change.

The development and application of remote-sensing algorithms for estimating the concentration of particulate organic carbon, POC [in units of mg m^{-3}], in surface waters from satellite observations of ocean color were initiated during the early years of operation of satellite mission of Sea-viewing Wide Field-of-View Sensor (SeaWiFS). The first POC algorithm was developed with field data from the Southern Ocean and was based on two empirical relationships linking the spectral remote-sensing reflectance of the ocean, $R_{rs}(\lambda)$ [sr^{-1}], with the spectral backscattering coefficient of seawater, $b_b(\lambda)$ [m^{-1}], and the particulate backscattering coefficient $b_{bp}(\lambda)$ with POC (where λ is light wavelength in vacuum and was chosen from the green spectral region in the first POC algorithm) (Stramski et al., 1999). During the following decade several studies examined POC algorithms based on various empirical approaches. In one category of algorithms, the formulation of algorithms was based on coincident field measurements of POC and optical variables including $R_{rs}(\lambda)$ and inherent optical properties (IOPs) of seawater (Allison et al., 2010b; Pabi and Arrigo, 2006; Stramska and Stramski, 2005; Stramski et al., 2008). Another category of algorithms was based on field measurements of POC and optical data that were not all collected in situ (satellite data products were included in the algorithm

development) or were not collected during the same field experiments (Gardner et al., 2006; Loisel et al., 2001; Loisel et al., 2002; Mishonov et al., 2003; Son et al., 2009). This latter category has limitations related to mismatch between the temporal and/or spatial scales in the determinations of variables involved in the algorithm formulation. More recently, a few alternative approaches with potential for global applications were proposed, specifically the estimation of POC from satellite-derived information on particle size distribution and relationship that converts particle size to carbon content (Kostadinov et al., 2016) and the estimation of POC from satellite-derived color index parameter (Le et al., 2018). In recent years, increased efforts have been also made with a focus on POC algorithms for coastal environments (Hu et al., 2016; Le et al., 2017; Liu et al., 2015; Tran et al., 2019; Woźniak et al., 2016). The coastal environments impose distinctive challenges for optically-based POC algorithms, which are associated primarily with generally much larger range of variability in proportions of organic and inorganic particles compared with open ocean environments (Woźniak et al., 2010). These challenges and the topic of remote-sensing of POC in such optically complex aquatic environments are beyond the scope of this study.

Several empirical algorithms in which POC is derived from measurements of $R_{rs}(\lambda)$ or from a combination of $R_{rs}(\lambda)$ and IOPs (especially the backscattering and beam attenuation coefficients) in open ocean environments were examined by Stramska and Stramski (2005) and Stramski et al. (2008). Given the field data available at that time, these studies suggested that the algorithm based on the blue-green band ratio of $R_{rs}(\lambda)$ is a reasonable candidate for applications to the global ocean where the vast extent of open-ocean waters is generally characterized by relatively low surface POC extending to about 300 mg m^{-3} . The NASA Ocean Biology Processing Group (OBPG) currently produces POC as a standard global ocean color product which is derived from the empirical relationship between surface POC and the blue-green band ratio of remote-sensing reflectance. This algorithm was originally determined for SeaWiFS band ratio of $R_{rs}(443 \text{ nm})/R_{rs}(555 \text{ nm})$ using POC and $R_{rs}(\lambda)$ measurements from the eastern South Pacific and Atlantic Oceans, which covered a range of surface POC from about 10 to 300 mg m^{-3} (Stramski et al., 2008). This band-ratio algorithm was also adopted by NASA OBPG to spectral bands of Moderate Resolution Imaging Spectroradiometer (MODIS) and Visible Infrared Imaging Radiometer Suite (VIIRS) ocean color sensors. NASA's implementation of these algorithms extends back to the beginning of the SeaWiFS mission in 1997. At present, a combination of SeaWiFS and subsequent ocean color missions, including MODIS-Terra and MODIS-Aqua as part of NASA-centered Earth Observing System (EOS) and VIIRS as part of NOAA/NASA partnership missions of Suomi National Polar-Orbiting Partnership (SNPP) and Joint Polar Satellite System (JPSS), provides over 20 years of continuous satellite data of global POC product.

As the EOS mission continues in its extended phase with SNPP serving as a bridge to the next generation JPSS, it is timely to reexamine and refine the global POC algorithms to ensure a continuity of multi-decadal POC data record based on observations with multiple satellite instruments. In the context of readiness of ocean satellite products as elements of a global ocean carbon observation system, POC was characterized as a product that should be exploited and further developed with subsequent need for global validation and selection of best algorithm (CEOS, 2014). This need was also supported in a recent study which examined the performance of several POC algorithms using a dataset of satellite-field matchups (Evers-King et al., 2017).

In the present study we examine numerous candidate approaches for formulating the empirical POC algorithms to allow the estimation of surface POC directly from spectral remote-sensing reflectance, $R_{rs}(\lambda)$. The primary goal is to obtain improved satellite instrument-specific algorithms for global applications, thereby preserving the backward continuity of satellite-derived POC data product, supporting the integration of the existing multi-satellite data record, and readying the algorithms for continued JPSS mission as well as Sentinel-3 mission of the European Space Agency (ESA). Specifically, we formulate the global

POC algorithms for SeaWiFS, MODIS (for both Aqua and Terra satellite missions), and VIIRS (for both SNPP and JPSS-1/NOAA-20 satellite missions) as well as for MEdium Resolution Imaging Spectrometer (MERIS) and Ocean and Land Colour Instrument (OLCI) on the ESA Envisat and Sentinel-3 satellite missions. Our effort builds on assembling a field dataset of particular relevance to the development of global POC algorithm. Specifically, the development dataset consists of nearly simultaneous and collocated measurements of $R_{rs}(\lambda)$ and POC in surface waters from a range of diverse and regionally-balanced environments within the global ocean, and is meant to cover a broader range of POC including polar regions which were not included in the current standard algorithm used by NASA OBPG. The presentation of our study consists of four main parts: (i) assembly of field dataset for the POC algorithm development, (ii) evaluation of numerous mathematical formulations for selecting the best candidate algorithms, (iii) description and characterization of final algorithms, and (iv) preliminary validation and example application.

2. Algorithm development dataset

2.1. Assembly of field dataset of POC and $R_{rs}(\lambda)$

Empirical relationships obtained from the regression analysis of the underlying experimental data provide the most straightforward approach to formulation of ocean color remote-sensing algorithms. Such empirical relationships depend on specific sets of data involved in the algorithm development, which has implications to the performance of algorithms within the scope of their intended use. Because our objective is to develop global POC algorithms, our approach to assembling an underlying field dataset of POC and $R_{rs}(\lambda)$ aims at creating a reasonably accurate representation of global relational patterns between these variables and hence allowing the determination of the representative average trendlines for the global ocean.

Generating such globally representative datasets is challenging because it requires the use of multiple sources of data which are often subject to differences in measurement and data processing methodologies. Recent efforts to compile large global databases from multiple data sources of in situ bio-optical measurements are described in Valente et al. (2016; 2019) and Aurin et al. (2018). Such efforts are intended to maximize the number of bio-optical data and their temporal and spatial distribution within a single unified database; for example in the database of Valente et al. (2019) coincident observations of Chla (chlorophyll-a concentration) and $R_{rs}(\lambda)$ are available at 3814 oceanographic stations compiled from numerous data sources with contributions by many investigators. Whereas such large diverse sets of data have been used to formulate global Chla algorithms, it is important to note that the probability distribution of bio-optical variables in these databases can differ considerably (e.g., Chla distribution shifted to larger values) compared with global distribution based on satellite-derived values and the scatter of data points in bio-optical relationships is usually very large, for example more than one order of magnitude variation in Chla at any given value of the spectral band ratio of $R_{rs}(\lambda)$ (O'Reilly and Werdell, 2019; Valente et al., 2019). In addition, because such large databases are created by merging multiple pre-existing processed datasets obtained using different instruments and different measurement and data processing methods, it is impossible to ensure that the same level of quality assurance and control is applied uniformly to all merged data. The process of merging large amounts of pre-existing datasets from various sources, with or without an attempt to conduct some data quality control, generally requires extensive automation and such merged datasets are unavoidably affected by varying degree of data quality and unpredictable uncertainties (Aurin et al., 2018; Valente et al., 2019). Probably the most unwanted effect on the development of empirical algorithms using such merged datasets is associated with the potential presence of subsets of data that are subject to unidentified methodological or measurement bias.

Compared to Chla and $R_{rs}(\lambda)$, coincident measurements of POC and $R_{rs}(\lambda)$ are less numerous but our initial investigation of such data from multiple public data sources indicated the potential presence of systematic differences in data patterns between different data sources (Stramski et al., 2006). In such cases it can be difficult or impossible to rule out the effects of methodological bias, at least in some datasets because of limited details in the available description of measurement and data processing protocols and/or the lack of replicate measurements. To address these limitations, in the present study we have taken a more targeted approach to assembling a dataset for development of global POC algorithms. Our approach does *not* aim at maximizing the number of coincident field observations of POC and $R_{rs}(\lambda)$ by merging data from all or nearly all available data sources. Instead, the key criteria used in our approach are focused on well-assured consistency and documentation of measurement protocols and well-balanced global representation of data in terms of both geographical coverage and range of bio-optical properties of seawater. The main goal is to have a dataset that can represent well an average trendline of global relationship between POC and $R_{rs}(\lambda)$ over a broader range of POC compared to that which was used to formulate the current standard POC algorithm. As a result of this approach we assembled a dataset consisting of 139 paired observations of $R_{rs}(\lambda)$ and near-surface POC collected during 15 cruises in diverse oceanic regions encompassing tropical, subtropical, and temperate latitudes as well as both the northern and southern polar latitudes. Fig. 1 depicts the locations of oceanographic stations where these measurements were made.

Field observations in the Pacific Ocean were obtained on two cruises. The BIOSOPE (Biogeochemistry and Optics South Pacific Experiment) cruise on the *R/V L'Atalante* sampled waters along a west-to-east transect in the eastern South Pacific Ocean between the Marquesas Islands and the coast of Chile from 17 October to 15 December 2004 (Claustre et al., 2008; Stramski et al., 2008). The KM12-10 cruise on the *R/V Kilo Moana* took place in tropical waters off the coast of Hawaiian Islands from 28 May to 10 June 2012 (Johnsen et al., 2014).

Field measurements in the Atlantic Ocean were conducted on two cruises on the *R/V Polarstern*. The ANTXXIII/1 cruise included the north-south transect in the eastern Atlantic between Germany and South Africa from 13 October to 17 November 2005 (Stramski et al., 2008). The ANTXXVI/4 cruise was along the transect from the southernmost part of Chile to Germany between 7 April and 17 May 2010 (Uitz et al., 2015). On this cruise the coincident POC and $R_{rs}(\lambda)$ data were collected along the southern portion of this transect.

Field data in the Indian Ocean were collected during the Arabian Sea Process Study (ASPS) as part of the U.S. Joint Global Ocean Flux Study (Smith et al., 1998). We use data from three cruises on the *R/V Thomas G. Thompson* in the Arabian Sea; TTN-045 from 14 March to 8 April 1995; TTN-053 from 29 October to 25 November 1995, and TTN-054 from 30 November to 26 December 1995. These cruises occurred during periods of Spring Intermonsoon, Fall Intermonsoon, and early Northeast Monsoon, respectively (Lee et al., 1998; Marra et al., 2000).

Field observations in the Southern Ocean were obtained during the Antarctic Environment and Southern Ocean Process Study (AESOPS) as part of the U.S. Joint Global Ocean Flux Study (Smith Jr. et al., 2000) and also during the U.S. Antarctic Marine Living Resources (AMLR) research program (Lipsky, 2001). The AESOPS data were collected in the Ross Sea during the NBP97-8 cruise on the *R/V Nathaniel B. Palmer* from 5 November to 13 December 1997 and two cruises (RR-KIWI 8 and RR-KIWI 9) on the *R/V Roger Revelle* in the Pacific sector of the Antarctic Polar Front Zone over the period 8 January – 19 March 1998 (Reynolds et al., 2001; Stramski et al., 1999). The AMLR2001 data were collected within a study area around the South Shetland Islands during the Leg 2 cruise of the 2000/2001 field season (8 February – 5 March 2001) on the Russian *R/V Yuzhmorgeologiya* (Hewes et al., 2001).

Field measurements in the western Arctic seas were made on four cruises. The MALINA (MAckenzie LIght aNd cARbon) cruise surveyed the southeastern Beaufort Sea during the period 31 July – 24 August 2009

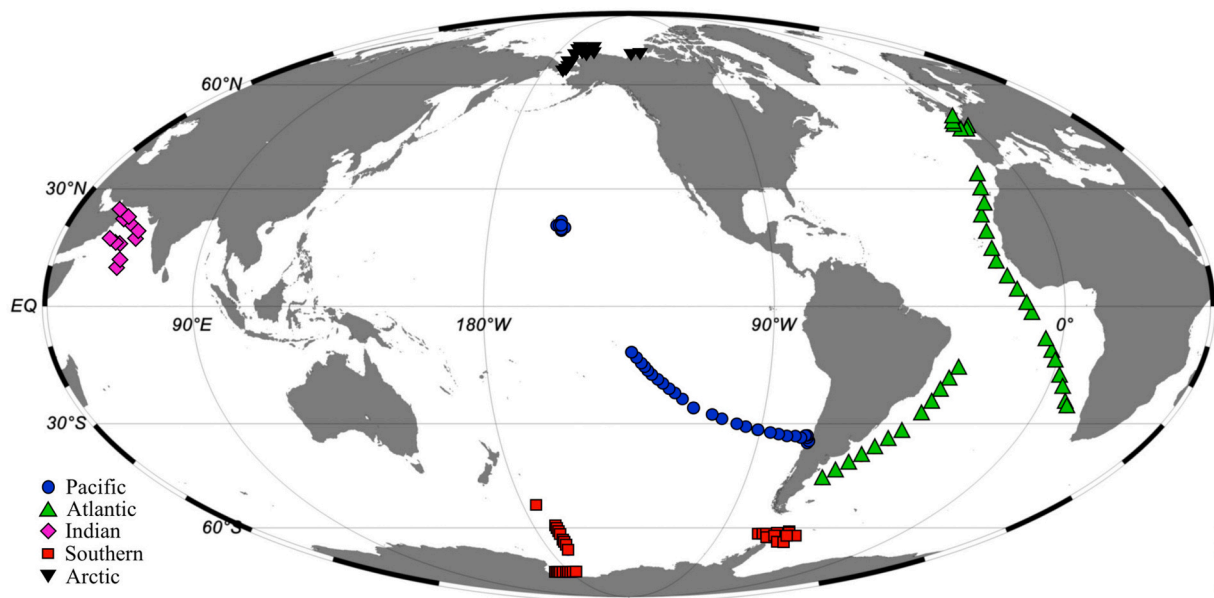


Fig. 1. Location of 139 oceanographic stations in major oceanic basins where coincident field data of spectral remote-sensing reflectance, $R_{rs}(\lambda)$, and surface concentration of particulate organic carbon, POC, were collected for the POC algorithm development dataset.

on the *CCGS Amundsen* (Antoine et al., 2013; Matsuoka et al., 2012). Two cruises on the *USCGC Healy* in the Chukchi Sea and western Beaufort Sea were associated with the NASA ICESCAPE (Impacts of Climate on EcoSystems and Chemistry of the Arctic Pacific Environment) program during two successive years; the HLY1001 cruise from 18 June through 16 July 2010 and HLY1101 from 28 June through 24 July 2011 (Arrigo, 2015; Reynolds and Stramski, 2019). The fourth Arctic cruise (MR17-05C) on the *R/V Mirai* sampled the Chukchi and Beaufort Seas over the period 23 August – 21 September 2017 (Shiozaki et al., 2019).

It is important to emphasize that not all paired observations of $R_{rs}(\lambda)$ and POC collected during the 15 cruises, which passed the data quality control process, were included in our algorithm development dataset. To create this final dataset, we applied additional inclusion criteria based on bio-optical and particle characteristics of seawater which are consistent with vast areas of open-ocean pelagic environments and hence most suitable for the development of global ocean algorithms. We used two threshold criteria involving the ratios of the absorption coefficient of chromophoric dissolved organic matter (CDOM), $a_g(412)$, to POC and Chla. Specifically, the final dataset includes data with $a_g(412)/\text{POC} \leq 0.00077 \text{ m}^2/\text{mg C}$ and $a_g(412)/\text{Chla} \leq 0.581 \text{ m}^2/\text{mg Chla}$. These threshold ratios were determined from the cruises in the Pacific and Atlantic Oceans where all measurements satisfied these inclusion criteria. Most data collected during the four Arctic cruises did not satisfy these CDOM-related criteria, which is indicative of relatively high concentrations of CDOM in these waters. This was also the case for some data from the NBP97-8 cruise in the Ross Sea and AMLR2001 cruise in the vicinity of the South Shetland Islands. In addition, some data from the Arctic were collected in waters dominated by mineral particles. To exclude such cases from our final dataset we disregarded data with the POC/SPM ratio less than 0.1 (where SPM is the mass concentration of suspended particulate matter). Such low values of POC/SPM are indicative of mineral-dominated particulate assemblages (Woźniak et al., 2010).

We also applied a bottom depth criterion in the creation of final dataset. One approach to avoid or minimize the effects associated with bio-optical complexity of coastal and shallow water environments would be to accept data collected only in deep pelagic environments off the continental shelf. However, given the available data such approach would limit the range of POC with a maximum value of only slightly

above 300 mg m^{-3} . Therefore, to cover a broader range of POC, we applied the inclusion criterion of bottom depth $\geq 50 \text{ m}$. This allowed us to include 16 observations from the Arctic waters and extend the maximum value of POC in the final dataset to above 1000 mg m^{-3} . Importantly, although these Arctic observations were collected on the continental shelf where bottom depth varied between 50 and 100 m, they all satisfied the CDOM-related and POC/SPM criteria that are consistent with data collected in open-ocean pelagic environments. Out of the total number of over 100 paired observations of $R_{rs}(\lambda)$ and POC collected on the four Arctic cruises, only these 16 observations satisfied all inclusion criteria used to create our final dataset. We also note that our POC algorithm development dataset includes measurements that were made over a broad range of solar zenith angle (θ_s) under clear skies, partly cloudy, or overcast conditions. For most observations (all Pacific, Atlantic, and Indian Ocean data except for one measurement in the Arabian Sea) the solar zenith angle was less than 60° and as low as 1° at one station during the BIOSOPE cruise. For the observations in the polar environments the lowest θ_s was about 43° and only 8 observations (out of the total of 50) were made at $\theta_s > 70^\circ$ generally under overcast conditions.

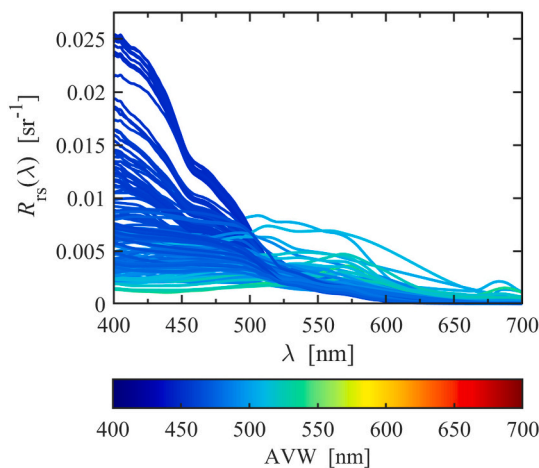
2.2. Characterization of field dataset

Table 1 provides a summary of measures of central tendency and the range of values for the Apparent Visible Wavelength (AVW), POC, and Chla based on observations from the five ocean basins separately and the final global dataset. The AVW (in units of nanometers) represents a simple metric that effectively characterizes the spectral shape of $R_{rs}(\lambda)$ (Vandermeulen et al., 2020). The mean and median values of AVW for our global dataset are about 460 nm. The AVW values as low as 433 nm were measured in ultraoligotrophic waters of the Pacific Ocean and the values as high as 530 nm in the Arctic waters. This is indicative of significant variation in the spectral shape of $R_{rs}(\lambda)$ within our dataset, which is illustrated in Fig. 2.

The POC and Chla values are, on average, lowest in the Pacific and Atlantic datasets, and highest in the Arctic dataset (Table 1). For example, the mean and median values of POC in the Pacific are about 54 and 31 mg m^{-3} , respectively, whereas in the Arctic these values are about 7-fold higher. For Chla, the differences in the mean or median values between the Pacific and Arctic datasets are even higher, more

Table 1Description and characterization of the final global dataset assembled for POC algorithm development. N is the number of paired radiometric and POC measurements.

Ocean basin	N	Research cruises	AVW [nm] Mean \pm SD (Median; Range)	POC [mg m^{-3}] Mean \pm SD (Median; Range)	Chla [mg m^{-3}] Mean \pm SD (Median; Range)
Pacific	38	BIOSOPE ($N = 30$) KM12–10 ($N = 8$)	445.3 \pm 15.9 (440; 433–484)	53.8 \pm 62.7 (31.1; 11.9–266.8)	0.22 \pm 0.39 (0.07; 0.02–1.48)
Atlantic	36	ANTXXIII/1 ($N = 24$) ANTXXVI/4 ($N = 12$)	454.4 \pm 12.6 (452.5; 435–494)	57.2 \pm 20.2 (54.0; 30.5–135.7)	0.26 \pm 0.18 (0.22; 0.09–1.01)
Indian	15	TTN045 ($N = 3$) TTN053 ($N = 4$) TTN054 ($N = 8$)	465.1 \pm 7.8 (463; 453–481)	76.5 \pm 32.6 (68.2; 46.9–159.0)	0.33 \pm 0.13 (0.31; 0.13–0.68)
Southern	34	NBP97–8 ($N = 9$) RR-KIWI 8 ($N = 8$) RR-KIWI 9 ($N = 2$) AMLR2001 ($N = 15$)	463.9 \pm 13.1 (462.5; 446–495)	96.2 \pm 70.9 (71.9; 20.6–315.6)	0.58 \pm 0.47 (0.44; 0.07–1.59)
Arctic	16	MALINA ($N = 2$) HLY1001 ($N = 6$) HLY1101 ($N = 4$) MRI7-05C ($N = 4$)	496.5 \pm 18.9 (499.5; 461–530)	377.4 \pm 318.6 (212.1; 67.2–1022.1)	4.99 \pm 6.36 (1.67; 0.09–19.60)
Combined	139		460.3 \pm 20.6 (458; 433–530)	104.8 \pm 153.4 (57.6; 11.9–1022.1)	0.88 \pm 2.59 (0.24; 0.02–19.60)

**Fig. 2.** Spectra of remote-sensing reflectance, $R_{rs}(\lambda)$, in the POC algorithm development dataset. Each given spectrum is color coded according to the value of Apparent Visible Wavelength (AVW) calculated from that spectrum.

than 20-fold. In the global dataset, the mean and median values of POC are about 105 and 58 mg m^{-3} , respectively. For Chla these values are 0.88 and 0.24 mg m^{-3} . The POC values span an 85-fold range from about 12 to 1022 mg m^{-3} and Chla covers approximately a 1000-fold range from 0.02 to 19.6 mg m^{-3} with the minimum in the ultraoligotrophic waters of South Pacific Gyre and maximum in the Arctic waters.

The probability distributions for the POC and Chla values in our POC algorithm development dataset are shown in Fig. 3. It is important to note that these probability density functions are consistent with results based on global satellite ocean color imagery, as also depicted in Fig. 3. The example monthly results of satellite-derived probability density functions of POC exhibit a maximum between about 30 and 50 mg m^{-3} and a median value of about 50 mg m^{-3} , which agree well with our algorithm development dataset (Fig. 3a, Table 1). For Chla the probability distributions are also consistent with probability maxima located between about 0.05 and 0.1 mg m^{-3} . The distributions based on our field dataset and the global satellite imagery also exhibit similar positive (right-tailed) asymmetry.

The relationship between POC and Chla also provides a useful characteristic of our dataset (Fig. 4). This relationship agrees well with a similar relationship derived from a large set of data collected within the euphotic layer of the pelagic ocean with bottom depths >300 m (Legendre and Michaud, 1999). The most frequently observed values of

POC/Chla ratio based on global satellite imagery are between 300 and 400 (Stramski et al., 2008) which is also consistent with the distribution of this ratio in our field dataset (not shown). Overall, the results in Figs. 3 and 4 support the representativeness of the assembled field dataset for the development of global POC algorithm.

3. Measurement methods

3.1. Measurements of $R_{rs}(\lambda)$

The spectral remote-sensing reflectance just above the sea surface, $R_{rs}(\lambda)$, is defined as a ratio $L_w(\lambda)/E_s(\lambda)$, where $L_w(\lambda) \equiv L_u(\lambda, z = 0^+)$ is the spectral water-leaving radiance with the vertical direction of photons travelling towards the zenith and $E_s(\lambda) \equiv E_d(\lambda, z = 0^+)$ is the spectral downwelling plane irradiance, and both quantities are defined just above the sea surface at $z = 0^+$. Table 2 provides background information on radiometric measurements during the different cruises included in this study. All determinations of $L_w(\lambda)$ were made from underwater measurements of spectral upwelling radiance, $L_u(\lambda, z)$, taken either at a single near-surface depth $z = 0.2$ m or from the vertical profile obtained within the ocean surface layer. The determinations of $E_s(\lambda)$ were made either directly from measurements of downwelling irradiance with an above-water sensor mounted on the vessel, or extrapolated from underwater vertical profile measurements of $E_d(\lambda, z)$ within the surface layer. These differences are associated with specific instruments and methods of deployment used on different cruises (Table 2).

The radiometric measurements and data processing are consistent with methods described in NASA and IOCCG protocols (Mueller and Austin, 1995; Mueller, 2003; IOCCG, 2019) although minor differences in details can occur between the cruises as different groups of investigators carried out the radiometric measurements on different cruises (see Supplementary Material). The references listed in Table 2 provide additional information on radiometric measurements and determinations of $R_{rs}(\lambda)$ data used in this study. Given that all $R_{rs}(\lambda)$ data were obtained consistently with in-water radiometry method following a protocol aimed at minimizing the overall measurement uncertainty due to various factors, such as instrument calibration and performance, deployment strategies, data reduction procedures, and effects of environmental conditions, it can be reasonably expected that the uncertainty of $R_{rs}(\lambda)$ in our dataset is typically of the order of 5% or less (IOCCG Protocol Series, 2019).

Table 2 also shows differences in the spectral coverage and wavelength interval between the cruises which depend on the radiometric instruments. Because our objective is to have the field data of $R_{rs}(\lambda)$ which are spectrally matched with the nominal wavelengths of the

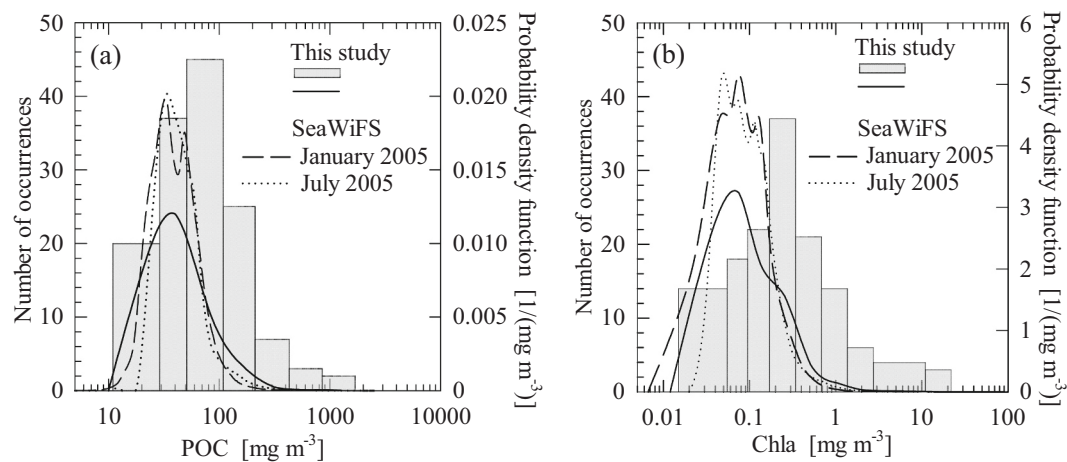


Fig. 3. Frequency distributions of (a) POC and (b) Chla for the POC algorithm development dataset and for examples of monthly composite data obtained from satellite observations with SeaWiFS. For the algorithm development dataset, the distributions are shown in terms of histograms (grey rectangles) and the corresponding probability density functions (solid lines). The width of histogram bins is variable to ensure a reasonably large number of occurrences within the bins (the total number of occurrences for the algorithm development dataset is 139). The satellite-based distributions are shown in terms of probability density functions (dashed and dotted lines). The satellite data of POC were derived with our SeaWiFS-specific hybrid algorithm described in Section 6. The satellite data of Chla represent the standard chlorophyll-a product generated by NASA OBPG.

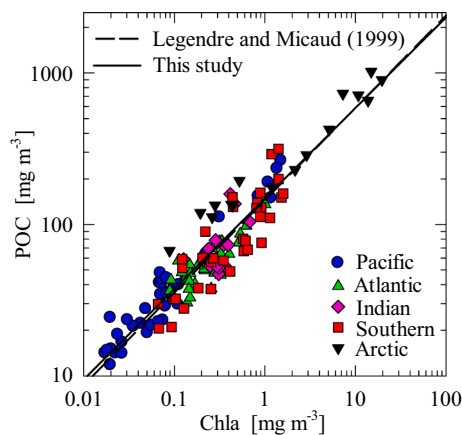


Fig. 4. The relationship between POC and Chla for the POC algorithm development dataset. The data from different oceanic basins are shown as indicated in the legend. The best-fit function for these data is $\log(\text{POC}) = 2.19 + 0.60 \log(\text{Chla})$. For comparison, the relationship $\log(\text{POC}) = 2.16 + 0.61 \log(\text{Chla})$ which was obtained by Legendre and Michaud (1999) is also shown.

standard $R_{rs}(\lambda)$ data products of different ocean color sensors, the data from each cruise were interpolated to a common wavelength interval of 1 nm between 400 and 700 nm. The linear interpolation was applied to measurements acquired at ~ 3.3 nm intervals with a HyperPro instrument. For all other $R_{rs}(\lambda)$ measurements obtained with multispectral radiometers the interpolation results were obtained using Piecewise Cubic Hermite Interpolating Polynomial (PCHIP) which produces no extraneous overshoots and wiggles compared with other cubic interpolation methods (Fritsch and Carlson, 1980). This interpolation approach was tested using hyperspectral data that were spectrally subsampled at appropriate wavelengths to create multispectral datasets simulating measurements with the multispectral radiometers. A very good agreement (to within a few percent) between the interpolated and measured data of $R_{rs}(\lambda)$ was found at the blue and green wavelengths required for development of POC algorithms for different ocean color sensors. For example, for the MODIS wavelength of 488 nm, the median absolute percentage difference (*MdAPD*) between the PCHIP interpolated and measured values of $R_{rs}(488)$ were less than 1% for all multispectral measurement scenarios that include SPMR, MER-2040, C-OPS,

and PRR-800 instruments. For the MODIS wavelength of 547 nm, the *MdAPD* values were also less than 1% with the exception of about 3% for the multispectral measurement scenario of MER-2040 that was used on the Arabian Sea cruises.

3.2. Measurements of POC

The POC determinations were based on routine methodology used in oceanography since 1960s, which consists of collection of discrete water samples at predetermined depths, filtration of samples (volumes up to about 10 L in clear waters) to accumulate the particulate matter on filters, and determination of carbon content on sample filters with a high-temperature combustion method (Menzel and Vaccaro, 1964). More specifically, all POC data included in this study were obtained with a method consistent with JGOFS protocols (Intergovernmental Oceanographic Commission, 1994) which were established before the oldest data in our dataset had been collected in the Arabian Sea in 1995. In brief, the key components of this method include filtration of water samples through precombusted 25 mm glass-fiber GF/F filters (Whatman) under low pressure differential across the filters, storage of dried or frozen filters until post-cruise analysis, and determination of organic carbon content with standard CHN analysis involving high temperature combustion of sample filters after removing inorganic carbon through acidification treatment. A number of unused blank filters from each lot of precombusted filters were used to quantify the average background amount of organic carbon on filters, which was then subtracted from the sample measurements. These blank filters were subject to the same steps of the protocol as sample filters except that no water was filtered through them. Surface water samples for POC determinations were collected within the near-surface layer typically between 2 m and 5 m depth using a Niskin rosette sampler. Few exceptions included two samples from the Arabian Sea (TTN-054 cruise) which were taken at 13 m and 20 m but still well within the surface mixed layer that extended to 40–60 m at these stations. Except for 15 POC samples from the Arabian Sea (Balch et al., 2000; Gundersen et al., 1998) and 2 samples from the MALINA cruise (Doxaran et al., 2012), the post-cruise analysis of all remaining POC samples was conducted at the Marine Science Institute (MSI) Analytical Lab, University of California Santa Barbara, using a CEC 440HA Elemental Analyzer (Control Equipment Corp., now Exeter Analytical) (Hewes et al., 2001; Reynolds et al., 2016; Stramski et al., 1999; Stramski et al., 2008).

To minimize uncertainties in POC determinations the measurement

Table 2
Instrumentation and deployment methods for collection of radiometric data in the final POC algorithm development dataset.

Research cruise	Instrument ^a	Deployment	Measured quantities	WI ^b	Spectral coverage	Reference
BIOSOPE ^c	HyperPro	Surface float	$L_u(z=0.2m), E_s(z=0^+)$	HS	350 – 800 nm at ~3.3 nm intervals	Stramski et al. (2008)
KM12-10 ^d	HyperPro	Surface float	as above	HS	as above	Johnsen et al. (2014)
ANTXXIII/1 ^d	SPMR	Depth profile	$L_u(z), E_d(z)$	MS	339, 380, 412, 443, 470, 490, 510, 532, 555, 590, 620, 666, 683 nm	Stramski et al. (2008)
ANTXXVI/4 ^d	HyperPro	Surface float	$L_u(z=0.2m), E_s(z=0^+)$	HS	350 – 800 nm at ~3.3 nm intervals	Uitz et al. (2015)
TTN045 ^c	MER-2040	Depth profile	$L_u(z), E_d(z)$	MS	412, 443, 490, 510, 555, 665 nm	U.S. JGOFS Data System $R_{rs}(\lambda)$ computed in this study
TTN053 ^c	MER-2040	Depth profile	as above	MS	as above	as above
TTN054 ^c	MER-2040	Depth profile	as above	MS	as above	as above
NBP97-8 ^{d,f}	MER-2040	Depth profile	$L_u(z), E_d(z)$	MS	340, 380, 395, 412, 443, 455, 490, 510, 532, 554, 570, 665 nm	Allison et al. (2010a)
RR-KIWI 8 ^{d,f}	MER-2040	Depth profile	as above	MS	as above	as above
RR-KIWI 9 ^{d,f}	MER-2040	Depth profile	as above	MS	as above	as above
AMLR2001 ^f	PRR-800	Depth profile	as above	MS	313, 320, 340, 380, 395, 412, 443, 465, 490, 510, 520, 532, 555, 565, 589, 625, 665, 710 nm	Hewes et al. (2001)
MALINA ^g	C-OPS	Depth profile	$L_u(z), E_d(z)$	MS	320, 340, 380, 395, 412, 443, 465, 490, 520, 532, 555, 560, 625, 665, 670, 683, 710, 780 nm	Antoine et al. (2013)
HLY1001 ^f	PRR-800	Depth profile	as above	MS	313, 320, 340, 380, 395, 412, 443, 465, 490, 510, 520, 532, 555, 565, 589, 625, 665, 710 nm	Zheng et al. (2014)
HLY1101 ^f	PRR-800	Depth profile	as above	MS	as above	as above
MR17-05C ^d	HyperPro	Surface float	$L_u(z=0.2m), E_s(z=0^+)$	HS	350 – 800 nm at ~3.3 nm intervals	Data processing as ANTXXVI/4

^a Instruments: HyperPro (Free-Falling Hyperspectral Optical Profiler, originally Satlantic, Inc., now SeaBird Scientific) with an in-water unit deployed as Hyper-spectral Tethered Spectral Radiometer Buoy (HyperTSRB); SPMR (SeaWiFS Profiling Multichannel Radiometer, Satlantic, Inc.); MER-2040 (Marine Environmental Radiometer, Biospherical Instruments, Inc.); C-OPS (Compact Optical Profiling System, Biospherical Instruments, Inc.); PRR-800 (Profiling Reflectance Radiometer, Biospherical Instruments, Inc.)

^b WI is the light wavelength interval of radiometric measurements where MS is multi-spectral and HS is hyperspectral.

^{c,e,f,g} Principal Investigators for radiometric data collection: M. R. Lewis, C. Trees, B. G. Mitchell, and S. B. Hooker, respectively.

^d Data collected by our team from the Ocean Optics Research Laboratory at Scripps Institution of Oceanography (SIO) (^{d,f} in collaboration with B. G. Mitchell).

protocol included sampling of water between the spigot and the bottommost part of the Niskin bottles to minimize the loss of particles due to settling, low vacuum during filtration (< 125 mmHg) to minimize potential loss of POC due to the impact of pressure differential across the filters, relatively large volumes of sample filtered to maximize the particulate carbon retained on the filter relative to background carbon, proper care during sample handling to reduce exposure to contamination, consistent acidification treatment to remove inorganic carbon from the samples, and determination of final POC values from replicate sample measurements. The average filtration volume ranged from about 1.5 L (\pm 0.6 L) for the Arctic cruises where the POC was highest to 5.6 L (\pm 2.4 L) for the Pacific cruises where the POC was lowest. Only one sample from the HLY1001 cruise in the Arctic was obtained with a filtration volume < 1 L and 12 out of 30 BIOSOPE samples were obtained with the largest volume of 8.4 L. The average and median ratio of organic carbon mass on sample filters to carbon mass on dry blank filters was about 25 and 15, respectively. These data are based on 229 sample filters (which include replicate sample filters) from the Pacific, Atlantic, Southern Ocean and Arctic cruises (the Arabian Sea, AMLR2001, and MALINA cruises excluded because of the lack of information on blank values). Multiple blank filters were taken on each cruise and the average and median values of carbon mass based on all blank filters were about 21 μ g C and 12 μ g C, respectively, which is consistent with earlier reports (e.g., Cetinić et al., 2012). Triplicate (at BIOSOPE stations) or duplicate (KM12–10, Atlantic, Arctic and some Southern Ocean stations) sample measurements were made and averaged to yield the final POC values. For 93 samples for which the replicate measurements were made the average and median values of the coefficient of variation (CV) are 6.8% and 4.7%, respectively. The CV was <10% for 77% of samples, <15% for 91% of samples, and < 25% for 97% of samples, which is indicative of generally good precision of POC determinations. The reproducibility can be also characterized by the absolute difference between the pair of replicates divided by the mean POC for the replicate measurements. The average and median values (in percent) for this quantity based on all pairs of replicates in our dataset are about 9% and 5%, respectively.

The accuracy of POC measurements is not exactly known and is likely variable among samples which is due to several sources of error which are impossible to completely eliminate and are difficult to accurately

quantify (IOCCG Protocol Series, 2021). It is, however, reasonable to assume that samples differing from one another by less than about 5 mg m^{-3} may not be resolved within current measurement uncertainties, which has particular ramifications for ultraoligotrophic waters where the lowest POC is less than 20 mg m^{-3} .

Potential sources of uncertainties in POC determinations have been reviewed by Gardner et al. (2003). The overestimation of POC resulting from adsorption of dissolved organic carbon (DOC) onto filters during filtration received special attention in previous studies which proposed the use of filtrate blank filters to account for DOC adsorption (Cetinić et al., 2012; Gardner et al., 2003; Menzel, 1966; Moran et al., 1999). Novak et al. (2018) examined an empirical relationship between the mass of DOC adsorbed onto the GF/F filter and the volume of sample filtered, which suggests that maximum DOC retention of about 30 μ g C is reached when more than about 0.6 L of seawater is filtered. These investigators also provided the exponential fit to experimental data of DOC retention as a function of filtration volume. Whereas this empirical function can provide a means for correcting the existing POC measurements obtained without the use of filtrate blank filters, it is notable that the data used in the exponential curve fitting in the study of Novak et al. (2018) exhibited substantial variability, generally more than 3-fold variation in DOC retention values at any filtration volume including the saturation region. Part of this variability may be associated with the nature of sample filtered (Abdel-Moati, 1990).

Despite these limitations, we examined this retroactive approach of DOC correction with our dataset obtained with the JGOFS protocol. We applied the DOC correction to 107 samples collected on all cruises except for the Arabian Sea, AMLR2001, and MALINA because information on the filtration volume for these cruises was not available. Our samples were obtained with relatively large filtration volumes of 3.7 ± 2.16 L (mean \pm standard deviation for 107 samples). Therefore, the DOC retention estimated from the exponential relationship of Novak et al. (2018) was similar for all samples, 30 ± 1.9 μ g C. The correction for these DOC-retention estimates in conjunction with our values of filter blanks reduced the values of POC in our dataset by 16% on average. The highest average reduction (~23% corresponding to about 7 mg m^{-3}) was associated with the data collected off the Hawaiian Islands on the KM12–10 cruise and the lowest reduction (~7–8% corresponding to

2–14 mg m⁻³) was associated with the Arctic data (Fig. 5). The POC values for the KM12–10 samples were very low, on average 32 mg m⁻³, compared with more than 10-fold higher average POC for the Arctic samples.

Whereas DOC adsorption is a source of positive bias (overestimation), there are several causes which can produce a negative bias (underestimation) of POC determined from seawater filtration using GF/F filters, such as incomplete retention of particles on filters, undersampling of rare large particles, and potential loss of POC due to the impact of pressure differential across the filters (Arthur and Rigler, 1967; Bishop and Edmond, 1976; Collos et al., 2014; Gardner, 1977; Gardner et al., 2003; Goldman and Dennett, 1985; Sharp, 1973; Sheldon, 1972). The retention of particulate matter on GF/F filters has critical significance because POC is operationally defined as a fraction of particulate organic carbon retained on a certain type of filter, such as the most commonly used glass-fiber GF/F filter with a nominal pore size of about 0.7 μm. Importantly, significant portion of small particles from submicrometer (colloidal) size range including viruses, bacteria, small picophytoplankton and organic detritus can pass GF/F filters (Li and Dickie, 1985; Lee and Fuhrman, 1987; Lee et al., 1995; Stramski, 1990; Taguchi and Laws, 1988) and, therefore, is excluded from routine determinations of POC on these filters. There is evidence that the fraction of POC that passes GF/F filters can be substantial; for example, Sharp (1973) reported that the organic colloidal fraction between 0.025 and 0.8 μm can contain more organic carbon than the particulate matter retained on the 0.8 μm pore size filters.

In the context of estimation of POC from ocean reflectance it is also important to recall that fine submicrometer particles are highly abundant in oceanic waters (Koike et al., 1990; Wells and Goldberg, 1992, 1994) and can make a significant contribution (>10%) to optical backscattering coefficient of suspended particles, especially in open-ocean environments (Stramski and Kiefer, 1991; Stramski and Woźniak, 2005; Zhang et al., 2020). As light backscattering is a major determinant of $R_{rs}(\lambda)$, colloidal particles which are missed by the standard POC method are likely to exert sizeable influence on $R_{rs}(\lambda)$. Thus, from the standpoint of both the optical algorithms and the representativeness of total POC pool in seawater, the most desirable approach would be to use POC data that include the contribution of colloidal particles. However, as yet no approach is available to routinely account for colloidal POC that is missed with the standard POC method.

Ideally, POC determinations should be corrected for all positive and

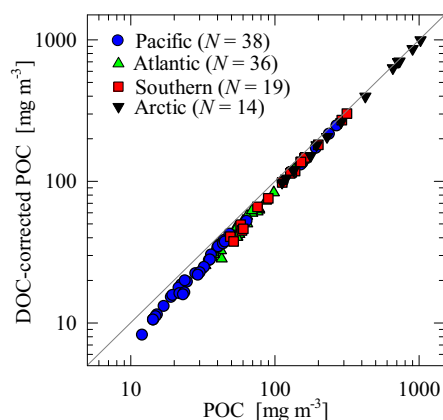


Fig. 5. The relationship between the POC values corrected for DOC adsorption according to the correction formula of Novak et al. (2018) and the original POC values in the POC algorithm development dataset. The number of stations, N , from each oceanic basin is indicated in the legend. This relationship is shown for a subset of 107 stations from the entire development dataset consisting of 139 stations (see text in Section 3.2 for details).

negative biasing effects; however, no standardized procedures presently exist to make such corrections (Gardner et al., 2003; Turnewitsch et al., 2007; IOCCG Protocol Series, 2021). The correction for a single source of bias does not necessarily reduce the final error if biasing effects with opposite sign remain uncorrected. It is thus conceivable that POC measurements corrected for DOC adsorption alone do not provide better estimates of the total POC (i.e., including the colloidal contribution) compared with measurements that are uncorrected for both an overestimation due to DOC adsorption and an underestimation due to missing colloidal POC. Consequently, if primary interest is in the total POC rather than operationally defined POC associated with particles that are strictly retainable on GF/F filters, the uncorrected measurements such as our POC dataset obtained with the JGOFS protocol without correction for DOC adsorption can be advantageous.

The subsequent descriptions of algorithm development and formulations in Sections 4, 5, and 6, as well as example validation and application results in Section 7 are presented for the original POC measurements (i.e., uncorrected for DOC) of the entire algorithm development dataset ($N = 139$). However, in Section 8 we include a table with the algorithms based on the subset of data with DOC-corrected POC values ($N = 107$) which is described above.

3.3. Ancillary measurements of Chla, SPM, and CDOM absorption coefficient

As described in Section 2.1 our final algorithm development dataset includes data that passed certain inclusion criteria which involved, in addition to POC, the measurements of Chla, SPM, and CDOM absorption coefficient, $a_g(\lambda)$, made on discrete surface seawater samples. The methods of these ancillary measurements are described elsewhere. In brief, Chla data from the Pacific, Atlantic, and Arctic cruises were made with High Performance Liquid Chromatography (HPLC) (Reynolds et al., 2016; Stramski et al., 2008; Uitz et al., 2015 and references therein). Chla data from the Southern Ocean were obtained using a fluorometric method for the AESOPS samples (Reynolds et al., 2001) and HPLC for the AMLR2001 samples (Hewes et al., 2001). The SPM measurements were used only in the process of selecting the Arctic data because some samples in our original Arctic database were characterized by relatively low organic vs. mineral contribution to particulate matter (i.e., low POC/SPM) and hence these samples were excluded from this study. The SPM measurements were made with a standard gravimetric method after collection of particulate matter by filtration onto GF/F filters (Reynolds et al., 2016). The absorption measurements of $a_g(\lambda)$ of the Pacific samples on the BIOSOPE cruise and the Arctic samples were made with an UltraPath instrument (Bricaud et al., 2010; Matsuoka et al., 2012). The Atlantic samples on the ANTXXIII/1 cruise were measured with a Point-Source Integrating-Cavity Absorption Meter, PSICAM (Röttgers and Doerffer, 2007) and the Southern Ocean samples with a spectrophotometric method using 10-cm pathlength quartz cuvettes (Reynolds et al., 2001).

4. Formulation and comparative analysis of various candidate algorithms

By applying a regression analysis to our algorithm development dataset consisting of field measurements of $R_{rs}(\lambda)$ and original POC (i.e., uncorrected for DOC adsorption), we examined seven distinct categories (CAT1 through CAT7) of algorithmic approaches. In each category we derived a number of alternative candidate formulas from a model-I regression between POC and an independent (explanatory) variable of X defined in terms of $R_{rs}(\lambda)$. The model-I regression is suitable because the objective of this analysis is to establish predictive relationships (e.g., Ricker, 1973; Sokal and Rohlf, 1995). In the comparative analysis of all candidate algorithms the best-fit coefficients of each regression formula were obtained using both the ordinary least squares method and a robust regression method with Tukey's bisquare weighting (Beaton et al., 1974;

Fox and Weisberg, 2011). The differences between the methods were small and the final algorithms reported in this paper are based on the robust regression method.

The key difference between the seven algorithmic categories is associated with fundamentally different definitions of X . For example, these definitions are based on the use of spectral band ratios of $R_{rs}(\lambda)$, the ratios of band differences of $R_{rs}(\lambda)$, or the differences between band ratios of $R_{rs}(\lambda)$. Within a given algorithmic category, the key differences between alternative formulas are associated with the number of spectral bands of $R_{rs}(\lambda)$ employed in the X variable, as well as the degree of polynomial function used to fit the data. This approach encompassing the seven algorithmic categories, each including multiple candidate formulas, was applied in essentially the same manner to specific sets of spectral bands of SeaWiFS, MODIS, VIIRS, MERIS, and OLCI sensors. For brevity, here we limit our description of algorithmic categories to SeaWiFS bands. Overall, the analysis of our development dataset with focus on SeaWiFS bands included over 70 candidate formulas across all seven algorithmic categories. The number of examined formulas differed between the categories ranging from 4 in CAT1 to 21 in CAT6.

For all algorithmic categories except Multiple Linear Regression (CAT7) the candidate algorithms were generated from the regression analysis applied to our dataset using the functional relationships that share one of these two general forms:

$$\log(\text{POC}) = f[\log(X)] \quad (1a)$$

$$\log(\text{POC}) = f[X] \quad (1b)$$

where \log is the logarithm with base 10 and f is a polynomial function of $\log(X)$ or X .

The CAT1 algorithms are referred to as BR-PF (Band Ratio-Power Function) and have the form:

$$\log(\text{POC}) = a_0 + a_1 \log(X) \quad (2)$$

where a_0 and a_1 are the best-fit coefficients, $X = R_{rs}(\lambda_1)/R_{rs}(555)$ and λ_1 is either 443, 490, or 510 nm. In this category we also considered X defined in terms of the maximum band ratio, $\text{MBR} = \max[R_{rs}(443)/R_{rs}(555), R_{rs}(490)/R_{rs}(555), R_{rs}(510)/R_{rs}(555)]$, which is a maximum value selected from the three band ratios. The current NASA standard POC algorithms belong to this category. For example, for the SeaWiFS bands the standard algorithm written in the form of power function is $\text{POC} = 203.2 [R_{rs}(443)/R_{rs}(555)]^{-1.034}$ (Stramski et al., 2008).

The CAT2 algorithms are referred to as MBR-OCx (Maximum Band Ratio-OCx) where x denotes the number of spectral bands involved in the algorithm formula. We considered the algorithms with 4, 5, and 6 bands, i.e., MBR-OC4, MBR-OC5, and MBR-OC6, respectively. These algorithms employ an approach that has been used in global ocean color (OC) chlorophyll algorithms (O'Reilly et al., 2000; O'Reilly and Werdell, 2019) and have the form:

$$\log(\text{POC}) = a_0 + \sum_{k=1}^n a_k [\log(X)]^k \quad (3)$$

where a_0 and a_k are the best-fit coefficients, $n = 3, 4$ or 5 denotes the degree of polynomial function, and $X \equiv \text{MBR}$ is the maximum band ratio. For the MBR-OC4 algorithm, $\text{MBR} = \max[R_{rs}(443)/R_{rs}(555), R_{rs}(490)/R_{rs}(555), R_{rs}(510)/R_{rs}(555)]$, for the MBR-OC5 the additional band ratio is $R_{rs}(412)/R_{rs}(555)$, and the MBR-OC6 includes also $R_{rs}(670)/R_{rs}(555)$. The $R_{rs}(670)/R_{rs}(555)$ ratio was, however, never selected as the maximum band ratio in our dataset.

The CAT3 algorithms are referred to as CI (Color Index) and have the form:

$$\log(\text{POC}) = a_0 + a_1 X \quad (4)$$

where $X \equiv \text{CI} = R_{rs}(555) - [R_{rs}(\lambda_1) + [(555 - \lambda_1)/(670 - \lambda_1)] [R_{rs}(670) - R_{rs}(\lambda_1)]]$ and λ_1 is either 443 or 490 nm. The CI approach builds upon a three-band reflectance difference concept which was originally

developed to improve chlorophyll algorithms in waters with low Chla (Hu et al., 2012). This concept was also recently tested for the estimation of POC by Le et al. (2018) but the CI-based formula was determined using satellite-derived $R_{rs}(\lambda)$ matched with in situ measurements of POC, rather than in situ dataset of paired $R_{rs}(\lambda)$ and POC measurements. We fitted Eq. (4) to our dataset within two ranges of CI, $< 0.0005 \text{ sr}^{-1}$ and $\geq 0.0005 \text{ sr}^{-1}$. This is consistent with the approach used by Le et al. (2018). As part of the CAT3 category, we also tested a combination of CI and MBR-OC4 algorithms following the concept applied to estimation of Chla (Hu et al., 2012). We used the POC range of 50–70 mg m^{-3} for the transition between the algorithms. The CI algorithm is used below 50 mg m^{-3} and the MBR-OC4 above 70 mg m^{-3} . Between these values, POC is estimated using a weighting approach similar to that used by Hu et al. (2012). Note also that according to Fig. 4 the POC range of 50–70 mg m^{-3} corresponds approximately to the Chla range of about 0.15–0.27 mg m^{-3} which is consistent with the transition range used in the NASA merged chlorophyll algorithm (O'Reilly and Werdell, 2019).

The CAT4, CAT5, and CAT6 algorithms have the same general form but differ in terms of the definition of X :

$$\log(\text{POC}) = a_0 + \sum_{k=1}^n a_k X^k \quad (5)$$

where n is 3, 4, or 5. In the CAT4 algorithms, which are referred to as NDCI (Normalized Difference Carbon Index), $X \equiv \text{NDCI} = [R_{rs}(555) - R_{rs}(\lambda_1)] / [R_{rs}(555) + R_{rs}(\lambda_1)]$ where λ_1 is either 443, 490, or 510 nm. In this category, we also examined additional variants of algorithms in which X is defined as a maximum value selected from the set of the three basic NDCIs. We note that the NDCI was previously used in POC algorithms in the study of the Gulf of Mexico (Son et al., 2009) and it conceptually resembles the Normalized Difference Vegetation Index (NDVI) that was originally developed for land vegetation (Deering et al., 1975; Rouse Jr. et al., 1973, 1974).

The next category of algorithms, CAT5, is referred to as mNDCI (minimum Normalized Difference Carbon Index). In this category, Eq. (5) operates with $X \equiv \text{mNDCI} = [R_{rs}(555) - \max(R_{rs}(\lambda_1), R_{rs}(\lambda_2), R_{rs}(\lambda_3))] / [R_{rs}(555) + \max(R_{rs}(\lambda_1), R_{rs}(\lambda_2), R_{rs}(\lambda_3))]$, where the "max" term represents a maximum reflectance selected from the three bands, $\lambda_1 = 412 \text{ nm}$, $\lambda_2 = 443 \text{ nm}$, and $\lambda_3 = 490 \text{ nm}$, or $\lambda_1 = 443 \text{ nm}$, $\lambda_2 = 490 \text{ nm}$, and $\lambda_3 = 510 \text{ nm}$. We also tested a variant with four wavelengths in the "max" term, 412, 443, 490, and 510 nm. Accordingly, the mNDCI represents a minimum value of the ratio of the difference between the green (555 nm) and blue (or blue-green) reflectance to their sum. We note that this index was used in the study of Son et al. (2009) but was referred to as "Maximum Normalized Difference Carbon Index" (MNDCI).

In the algorithmic category CAT6, referred to as BRDI (Band Ratio Difference Index), Eq. (5) was examined with three basic variants of $X \equiv \text{BRDI}$ as follows: (i) $[R_{rs}(443) - R_{rs}(555)] / [R_{rs}(490)]$, (ii) $[R_{rs}(443) - R_{rs}(555)] / [R_{rs}(510)]$, and (iii) $[R_{rs}(490) - R_{rs}(555)] / [R_{rs}(510)]$. In addition, in this category we examined four additional variants of X defined in terms of the Maximum Band Ratio Difference Index (MBRDI). One variant of MBRDI represents a maximum value selected from the three basic BRDI variants. Each of the three remaining variants of MBRDI selects a maximum value from a different combination of two basic BRDI variants.

The CAT7 algorithms are based on Multiple Linear Regression (MLR) approach in which we used reflectances at two or three bands. For example, a 2-band version has the form:

$$\log(\text{POC}) = a_0 + a_1 R_{rs}(\lambda_1) + a_2 R_{rs}(\lambda_2) \quad (6)$$

In this version we examined two combinations of λ_1 and λ_2 , 443 and 555 nm, and 490 and 555 nm. A 3-band version of MLR has an additional term $a_3 R_{rs}(\lambda_3)$ where $\lambda_3 = 670 \text{ nm}$. We tested four variants of the 3-band MLR with the following pairs of λ_1 and λ_2 : 443 and 510 nm, 443 and 555 nm, 490 and 510 nm, and 490 and 555 nm. We note that similar MLR

approach was previously applied in the POC algorithm in the study of the Louisiana continental shelf (Le et al., 2017).

Several statistical measures describing the goodness-of-fit of regression functions for our development dataset were used in comparative analysis of numerous candidate algorithms, which aimed at selecting a few top candidate algorithms (Table 3). These measures are generally consistent with a suite of parameters commonly used in comparisons between modelled (e.g., algorithm-derived) and reference (e.g., measured) data involving ocean biogeochemical or bio-optical variables (Brewin et al., 2015; Doney et al., 2009; Friedrichs et al., 2009; Seegers et al., 2018; Stow et al., 2009). We found that the residual differences between the algorithm-derived and measured POC were characterized by nearly symmetric probability distributions with a maximum near zero. The *MdR* and *MdB* characterize systematic deviations, and the *MdAPD* and *RMSD* random deviations between the algorithm-derived POC and measured POC for the development dataset. The algorithms that provide the best overall fit to measured data have *MdR* close to 1 and low values (the closer to zero the better) of *MdB*, *MdAPD* and *RMSD*. The errors of bio-optical models are often characterized by statistical indicators calculated in logarithmic space (Campbell et al., 2002; Seegers et al., 2018). Such indicators were also calculated for our analysis (see Table 3) and were consistent with information provided by statistics calculated in linear space.

A model-II linear regression analysis based on the reduced major axis method (Kermack and Haldane, 1950; Ricker, 1973) was also applied to algorithm-derived POC vs. measured data of POC after logarithmic transformation of POC data. The best-fit coefficients of this regression function and the correlation coefficient (Table 3) aid in the assessment of the degree to which the algorithm-derived POC agrees with measured POC over the entire dynamic range. For example, the deviation of the slope *S* of the fitted regression from 1 can reveal the variation in the bias of algorithm-derived POC relative to measured POC across the range of measured values. The potential presence of bias at different ranges of POC was examined with plots of the difference between the algorithm-derived and measured POC vs. measured POC, which is similar to the Bland Altman analysis (Altman and Bland, 1983; Bland and Altman, 1983).

In addition, we conducted a pair-wise comparison analysis for comparing the skill of candidate algorithms (Seegers et al., 2018). In this analysis, the differences between the algorithm-derived and measured POC were calculated for each observation for each pair of algorithms involved in a pair-wise comparison. The algorithm with more wins (i.e., higher number of smallest differences) is considered superior. For each algorithmic category all possible pairs of candidate algorithms were subject to this analysis, and the algorithms were ranked according to the number of wins. Together, all computed statistical indicators including the ranking from pair-wise comparisons provided a suite of decision metrics for selecting the best candidate algorithm from each algorithmic category. The selected algorithms from each category were then subject

Table 3
Statistical metrics used in comparative assessment of candidate algorithms.

Symbol	Description
<i>N</i>	Number of samples
y_i, x_i	Algorithm-derived <i>y</i> and measured <i>x</i> value for sample <i>i</i> of <i>N</i>
<i>R</i>	Pearson's product moment correlation coefficient
<i>MdR</i>	Median ratio; median value of (y_i / x_i)
<i>MdB</i>	Median bias; median value of ($y_i - x_i$)
<i>MdAPD</i>	Median absolute percentage difference; median value of $100 \times [(y_i - x_i) / x_i]$
<i>RMSD</i>	Root mean square deviation calculated as $[(1/N) \sum_{i=1}^N (y_i - x_i)^2]^{0.5}$
<i>S</i> and <i>A</i>	Exponent and multiplicative coefficients of power function, $y = A x^S$, obtained from model-II linear regression of $\log(y_i)$ on $\log(x_i)$ (<i>S</i> is equivalent to the slope of linear function between log-transformed variables and $A = 10^I$ where <i>I</i> is the intercept of this linear function)
<i>MdAE_{log}</i>	Median absolute error calculated as $10^{\text{median}(\log(y_i) - \log(x_i))}$
% wins	Percentage wins in pairwise comparisons of y_i and x_i from multiple models

to similar comparative analysis which eventually resulted in the selection of a few best candidates for formulating the final algorithms. In brief, this selection was based upon consideration of a suite of multiple statistical metrics which were obtained by analyzing the entire development dataset as well as different subranges of POC within the dataset. The behavior of different algorithms at low POC was also considered.

A summary of the results describing the comparative analysis of all candidate algorithmic categories is presented in Supplementary Material. Table S1 shows the best-fit regression functions from each algorithmic category for our algorithm development dataset. Fig. S1 illustrates the regression functions for different algorithmic categories and all data comprising our dataset. Tables S2 and S3 provide the goodness-of-fit statistical parameters and selected pair-wise comparison results for the best-fit regression functions from different algorithmic categories. The comparative analysis of different candidate algorithms resulting in selection of algorithms from CAT2 and CAT6 as most suitable for formulation of final algorithms is described in detail in Supplementary Material.

5. Characterization of selected candidate algorithms

The MBR-OC4 cubic polynomial function (Eq. 3) from CAT2 and BRDI quintic polynomial function (Eq. 5) from CAT6 were used in further analysis aimed at formulating the final algorithms. For brevity, we here limit the presentation of these algorithms to the case of SeaWiFS bands. For this sensor the MBR-OC4 is based on the 443, 490, 510, and 555 nm bands. The BRDI algorithm also involves these four bands with BRDI defined as a maximum value selected from two individual BRDIs, $[R_{rs}(443) - R_{rs}(555)] / R_{rs}(490)$ and $[R_{rs}(490) - R_{rs}(555)] / R_{rs}(510)$. Thus, this BRDI formulation is hereafter referred to as MBRDI. For comparison, we also illustrate the best algorithm from the BR-PF category because, despite its inferior goodness-of-fit statistics for our development dataset, this algorithm is consistent with the current formulation of the NASA standard POC algorithm based on the single blue-to-green band ratio $R_{rs}(443)/R_{rs}(555)$.

Fig. 6 shows the best fit function of BR-PF algorithm for our dataset and the relationship between the algorithm-derived and measured POC including the values of statistical indicators. As seen, this algorithm tends to overestimate the measurements at very low POC and underestimate at high POC (Fig. 6b). The power function with the best-fit coefficients used in the current standard NASA algorithm also exhibits similar features, as shown for comparison (Fig. 6a). In addition, the $R_{rs}(443)/R_{rs}(555)$ ratio corresponding to hypothetical ocean consisting of pure seawater only is indicated in Fig. 6a. This value was obtained from radiative transfer simulations assuming a solar zenith angle of 30° and a wind speed of 5 m s⁻¹ (Li et al., 2016). The BR-PF fitted line has the band ratio value of pure ocean at POC significantly above zero (~12 mg m⁻³).

Fig. 7 provides similar results but for the MBR-OC4 algorithm which is clearly superior to BR-PF in terms of representing the dataset over the entire dynamic range of measurements. For the MBR-OC4 algorithm the values of *S*, *A*, and *MdR* are all very close to 1, and *MdAPD* is quite low, 13.8% (Fig. 7b). The *RMSD* value of 41.7 mg m⁻³ is also significantly reduced compared with 75.4 mg m⁻³ for the BR-PF algorithm. Better performance of MBR-OC4 at high POC is primarily attributable to the fact that the function employed in the MBR-OC4 algorithm better captures the behavior of high POC data than the BR-PF formula. With regards to very low POC less than about 20 mg m⁻³, the MBR-OC4 algorithm tends to overestimate the measurements in our dataset. Also, this algorithm predicts POC of about 10 mg m⁻³ when the MBR value corresponds to pure seawater condition.

Fig. 8 depicts results for the MBRDI algorithm. In general, the statistical indicators of MBRDI calculated for the entire dynamic range are similar to those of MBR-OC4 algorithm (Fig. 8b). A comparative analysis of statistical indicators for MBR-OC4 and MBRDI over different ranges of POC indicated, however, that the MBR-OC4 provided slightly better

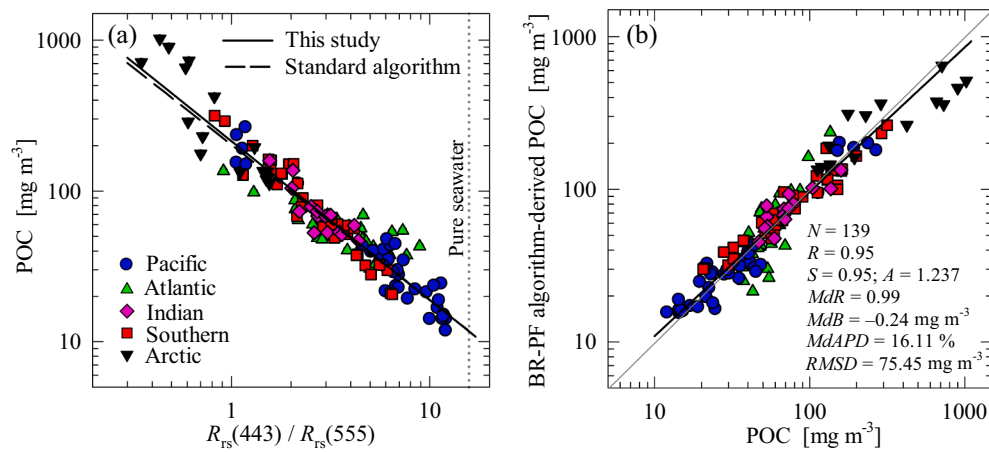


Fig. 6. BR-PF (Band Ratio Power Function) algorithm for SeaWiFS based on the POC algorithm development dataset. (a) POC as a function of remote-sensing reflectance band ratio, $R_{rs}(443)/R_{rs}(555)$. Shown are the best-fit power function for the algorithm development dataset (solid line) and, for comparison, the current standard POC algorithm used by NASA OBPG (dashed line). An approximate value of $R_{rs}(443)/R_{rs}(555)$ for the case of pure seawater (dotted line) is also shown. (b) The BR-PF algorithm-derived POC vs. measured POC for the algorithm development dataset. A model-II regression line fit to the log-transformed data (black solid line) and the 1:1 line (thin grey line) are shown along with several statistical parameters. The data from different oceanic basins are depicted as indicated in panel (a).

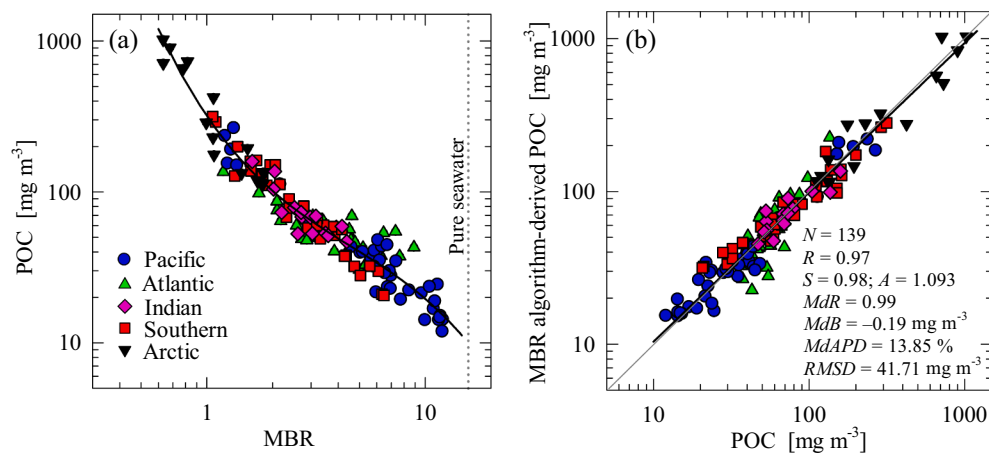


Fig. 7. MBR-OC4 (Maximum Band Ratio-Ocean Color 4) algorithm for SeaWiFS based on the POC algorithm development dataset. (a) POC as a function of MBR. The best-fit cubic polynomial function for the algorithm development dataset (solid line) and approximate value of MBR for the case of pure seawater (dotted line) are shown. (b) The MBR-OC4 algorithm-derived POC vs. measured POC for the algorithm development dataset. A model-II regression line fit to the log-transformed data (black solid line) and the 1:1 line (thin grey line) are shown along with several statistical parameters. The data from different oceanic basins are depicted as indicated in panel (a).

representation of data at high POC > 100 mg m⁻³ and MBRDI provided a better representation of data at very low POC, especially < 20 mg m⁻³. The differences in the goodness-of-fit at intermediate values of POC are smaller and not so apparent. Compared with MBR-OC4, the MBRDI formulation has two notable features; it better represents the measurements at very low POC and predicts POC significantly closer to zero (~1.5 mg m⁻³) when the explanatory variable of MBRDI corresponds to pure seawater condition.

This analysis suggests that a hybrid algorithm which combines the

MBR-OC4 and MBRDI formulas with the latter operating only in ultra-oligotrophic waters with very low POC is the best candidate approach for global POC algorithm. We recall that in this variant of MBRDI, the MBRDI values are selected from two BRDIs, $[R_{rs}(443) - R_{rs}(555)] / R_{rs}(490)$ and $[R_{rs}(490) - R_{rs}(555)] / R_{rs}(510)$. In our dataset the first BRDI is always selected when POC is less than about 25 mg m⁻³. The second BRDI, which involves the 510 nm band, is selected for almost all remaining data. This indicates that for ultraoligotrophic waters, the MBRDI formula can be replaced with the BRDI formula involving

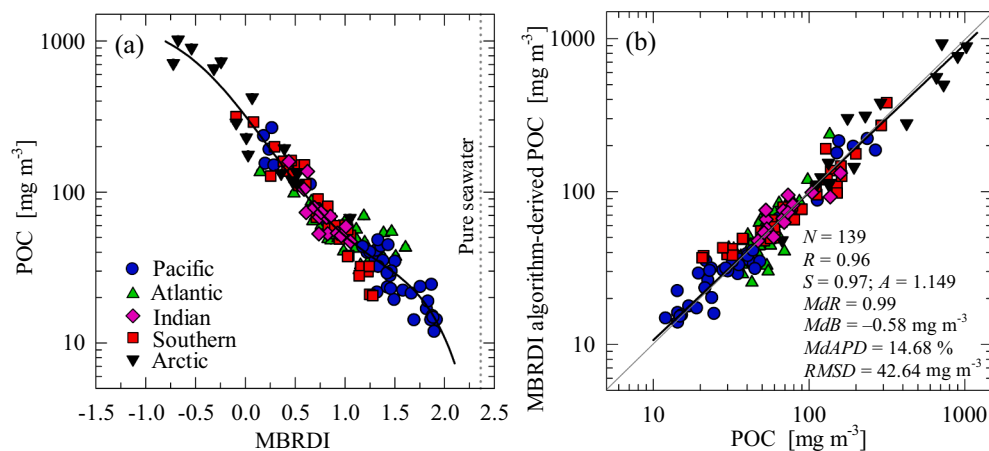


Fig. 8. MBRDI (Maximum Band Ratio Difference Index) algorithm for SeaWiFS based on the POC algorithm development dataset. (a) POC as a function of MBRDI. The best-fit quintic polynomial function for the algorithm development dataset (solid line) and approximate value of MBRDI for the case of pure seawater (dotted line) are shown. (b) The MBRDI algorithm-derived POC vs. measured POC for the algorithm development dataset. A model-II regression line fit to the log-transformed data (black solid line) and the 1:1 line (thin grey line) are shown along with several statistical parameters. The data from different oceanic basins are depicted as indicated in panel (a).

$[R_{rs}(443) - R_{rs}(555)] / R_{rs}(490)$. This approach eliminates a need to use BRDI involving the 510-nm band.

Towards this end, we tested several candidate formulas of BRDI algorithm based on polynomial functions which relate POC to $BRDI = [R_{rs}(443) - R_{rs}(555)] / R_{rs}(490)$. The goal of this analysis was to establish the BRDI algorithm for use within a range of very low POC less than about 25 mg m^{-3} , and most importantly below 20 mg m^{-3} . We tested the candidate BRDI formulas using different subsets of our data with POC extending beyond a desired range of BRDI applicability. For example, the curve fitting was done for $POC < 50$, < 60 , < 70 , and $< 100 \text{ mg m}^{-3}$. This approach ensured that the fitted functions conform to general pattern of reasonably good number of data over reasonably large dynamic range covering relatively low POC. In contrast, the curve fitting over a subset of data limited to only very low POC, such as $< 25 \text{ mg m}^{-3}$, would be at high risk of obtaining spurious results because the number of data within this narrow range is relatively small ($N = 18$) and these data exhibit significant scatter that can be attributed, at least partly, to increased relative error in measurements of very low POC. As a result of this analysis, the quintic polynomial function (Eq. 5) fitted to data within the range of $POC < 70 \text{ mg m}^{-3}$ ($N = 89$) was selected as the final BRDI formula (Fig. 9a). The BRDI functions fitted for $POC < 50$ or $< 100 \text{ mg m}^{-3}$ were found to be similar to the selected BRDI formula within the middle section of the considered POC range, but they exhibited less desirable behavior at the high or low ends of the data range (not shown). Importantly, the selected BRDI algorithm produces the POC values in very good agreement with the MBRDI algorithm at low POC up to about 40 mg m^{-3} (Fig. 9b). In addition, similar to the MBRDI algorithm (Fig. 8a), the selected BRDI function shown in Fig. 9a attains the pure seawater condition at very low POC ($\sim 0.27 \text{ mg m}^{-3}$). This feature is advantageous compared with other algorithms which predict POC significantly above zero at pure seawater condition ($\sim 10 \text{ mg m}^{-3}$ or higher depending on the algorithm, see Supplementary Material). Owing to this feature the BRDI algorithm allows estimation of POC down to the lowest values of POC found in surface waters of ultraoligotrophic ocean (which are about 10 mg m^{-3} or perhaps even below 10 mg m^{-3}) while the BRDI value does not yet reach the pure seawater condition.

6. Formulation of final hybrid algorithms

The approach to formulate a hybrid algorithm by merging the MBR-OCx and the BRDI formulas is the same for the six satellite sensors considered in this study. The coefficients of all final hybrid algorithms and the weighting approach used to create the hybrid algorithms are

displayed in Table 4. Table S4 (Supplementary Material) provides the goodness-of-fit statistical parameters for all final hybrid algorithms presented in Table 4.

The hybrid algorithm consists of the use of MBR-OC4 formula when $POC > 25 \text{ mg m}^{-3}$ and the BRDI formula when $POC < 15 \text{ mg m}^{-3}$. We note that for the algorithms that use MBR-OC4v or MBR-OC3 the general algorithmic scheme is analogous. A weighting approach is used in the transition range of $15 \leq POC \leq 25 \text{ mg m}^{-3}$ (Table 4). First, the initial weighting factors w_{MBR} and w_{BRDI} for the MBR-OC4 and BRDI formulas are determined. Note that whereas w_{MBR} increases logarithmically from 0 to 1 as POC_{MBR} increases from 15 to 25 mg m^{-3} , w_{BRDI} decreases from 1 to 0 within this range. The BRDI weighting factor declines quite rapidly, for example to about 0.25 at POC_{BRDI} of 20 mg m^{-3} , which is consistent with a desired dominant role of BRDI in the hybrid algorithm only at very low POC. The w_{MBR} and w_{BRDI} factors assume the value of 0.5 when POC_{MBR} or POC_{BRDI} is about 17.4 mg m^{-3} , which is also indicative of a dominant role of w_{MBR} over most of the transition region.

Because w_{MBR} and w_{BRDI} are calculated independently using POC estimated from two different algorithms, the sum of these initial weighting factors is generally not equal to 1. The final weighting factors, W_{MBR} and W_{BRDI} , are calculated to satisfy the condition that their sum is equal to 1. Using W_{MBR} and W_{BRDI} in the final step of the hybrid algorithm, POC is calculated as the weighted sum of POC_{MBR} and POC_{BRDI} . This weighting approach was designed to operate for any combination of the POC_{MBR} and POC_{BRDI} pair regardless of whether both or any of the two values are within or outside the transition region between 15 and 25 mg m^{-3} , and regardless of whether the “outside” value(s) are above or below the boundaries of the transition region.

As intended, POC_{BRDI} begins to be lower than POC_{MBR} for POC less than about 20 mg m^{-3} where the BRDI contribution to the hybrid algorithm is dominant. For $POC > 20 \text{ mg m}^{-3}$ the MBR-OC4 makes a dominant or total contribution to the hybrid algorithm, but both algorithms provide similar POC output up to $40\text{--}50 \text{ mg m}^{-3}$ although with a tendency for POC_{BRDI} to be somewhat higher than POC_{MBR} , especially between 20 and 30 mg m^{-3} (not shown). In this range, however, the MBR-OC4 makes a dominant contribution to the hybrid algorithm. In addition, POC_{BRDI} remains very close to POC_{MBR} in the range from about 30 mg m^{-3} to 50 mg m^{-3} . As shown in Fig. 9a POC_{BRDI} is, on average, about 45 mg m^{-3} when $BRDI = 1$. In accordance with these features, we apply an initial condition to the hybrid algorithm which is $POC = POC_{MBR}$ if $BRDI < 1$ (Table 4). This condition implies that the hybrid algorithm proceeds with the calculation of weighting factors and the weighted estimate of POC only when $BRDI \geq 1$. The main rationale for

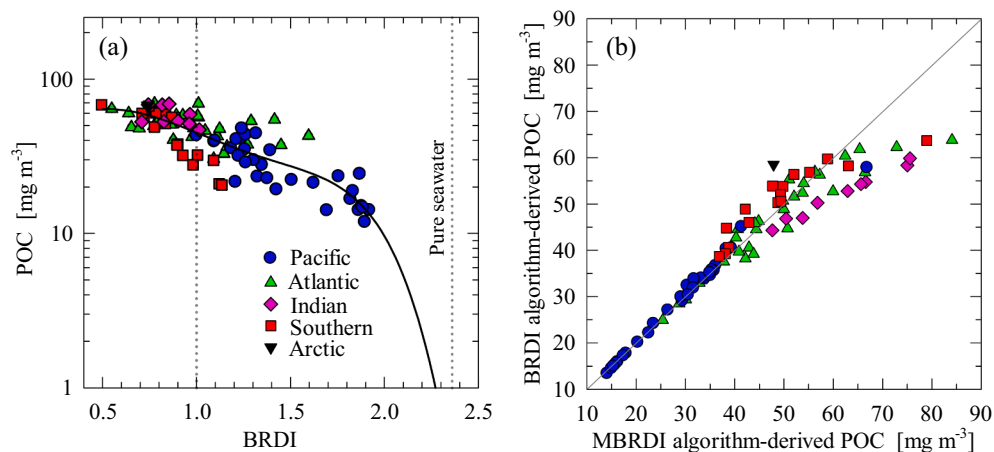


Fig. 9. BRDI (Band Ratio Difference Index) algorithm for SeaWiFS based on the subset of data from the POC algorithm development dataset which encompasses the range of $POC < 70 \text{ mg m}^{-3}$ (the number of subset data $N = 89$). (a) POC as a function of BRDI. The best-fit quintic polynomial function for the subset of algorithm development dataset (solid line) and approximate value of BRDI for the case of pure seawater (dotted line) are shown. In addition, the vertical dotted line at $BRDI = 1$ is shown to indicate the lower limit of the range of BRDI values that are used in the hybrid algorithm (see text in Section 6 for details). (b) The BRDI algorithm-derived POC vs. MBRDI algorithm-derived POC for the subset of algorithm development dataset. The 1:1 line (thin grey line) indicates a very good agreement between the two algorithms in the range of low POC values intended for application of BRDI algorithm. The data from different oceanic basins are depicted as indicated in panel (a).

Table 4

Final hybrid algorithm formulations and parameter values based on the algorithm development dataset with original POC measurements ($N = 139$).

Algorithm	Reflectance band parameter	a_0	a_1	a_2	a_3	a_4	a_5
<i>SeaWiFS hybrid algorithm</i>							
MBR-OC4 ^a	MBR = max[$R_{rs}(443, 490, 510)/R_{rs}(555)$]	2.5037	-2.1297	1.8727	-0.9554		
BRDI ^b	BRDI = [$R_{rs}(443) - R_{rs}(555)$] / $R_{rs}(490)$	1.5407	0.8586	-0.0787	-1.8571	1.5738	-0.3839
<i>MODIS hybrid algorithm^c</i>							
MBR-OC3	MBR = max[$R_{rs}(443, 488)/R_{rs}(547)$]	2.4500	-2.0920	1.8148	-0.9726		
MBR-OC4v ^d	MBR = max[$R_{rs}(443, 488, 510v)/R_{rs}(547)$] where $R_{rs}(510v) = 0.5 R_{rs}(510_A) + 0.5 R_{rs}(510_B)$; $R_{rs}(510_A) = -0.00008 + 1.085 R_{rs}(488)$ and $R_{rs}(510_B) = -0.00041 + 1.104 R_{rs}(531)$ $R_{rs}(510v)$ is used only when $R_{rs}(510v)/R_{rs}(547) < 1.2$, $R_{rs}(510v) > R_{rs}(443)$, and $R_{rs}(510v) > R_{rs}(488)$	2.5155	-2.5893	2.8241	-1.5640		
BRDI	BRDI = [$R_{rs}(443) - R_{rs}(547)$] / $R_{rs}(488)$	1.6876	0.0936	1.6170	-3.9144	2.8003	-0.6633
<i>VIIRS-SNPP hybrid algorithm^c</i>							
MBR-OC3	MBR = max[$R_{rs}(443, 486)/R_{rs}(551)$]	2.4484	-1.9178	1.4910	-0.7694		
MBR-OC4v	MBR = max[$R_{rs}(443, 486, 510v)/R_{rs}(551)$] where $R_{rs}(510v) = 0.63 R_{rs}(510_A) + 0.37 R_{rs}(510_B)$; $R_{rs}(510_A) = -0.000070 + 1.096 R_{rs}(486)$ and $R_{rs}(510_B) = -0.00094 + 1.221 R_{rs}(551)$ $R_{rs}(510v)$ is used only when $R_{rs}(510v)/R_{rs}(551) < 1.2$, $R_{rs}(510v) > R_{rs}(443)$, and $R_{rs}(510v) > R_{rs}(486)$	2.5274	-2.4977	2.6253	-1.4109		
BRDI	BRDI = [$R_{rs}(443) - R_{rs}(551)$] / $R_{rs}(486)$	2.0748	-2.3225	7.2895	-10.1575	6.0496	-1.3119
<i>VIIRS-JPSS-1 hybrid algorithm^c</i>							
MBR-OC3	MBR = max[$R_{rs}(445, 489)/R_{rs}(556)$]	2.4596	-1.8083	1.3031	-0.6740		
MBR-OC4v	MBR = max[$R_{rs}(445, 489, 510v)/R_{rs}(556)$] where $R_{rs}(510v) = 0.69 R_{rs}(510_A) + 0.31 R_{rs}(510_B)$; $R_{rs}(510_A) = -0.0000004 + 1.068 R_{rs}(489)$ and $R_{rs}(510_B) = -0.00130 + 1.291 R_{rs}(556)$ $R_{rs}(510v)$ is used only when $R_{rs}(510v)/R_{rs}(556) < 1.2$, $R_{rs}(510v) > R_{rs}(445)$, and $R_{rs}(510v) > R_{rs}(489)$	2.5213	-2.2566	2.1640	-1.1510		
BRDI	BRDI = [$R_{rs}(445) - R_{rs}(556)$] / $R_{rs}(489)$	2.5909	-4.9681	12.3141	-14.4830	7.7375	-1.5461
<i>MERIS and OLCI hybrid algorithms</i>							
MBR-OC4	MBR = max[$R_{rs}(442.5, 490, 510)/R_{rs}(560)$]	2.5013	-1.9388	1.5255	-0.7507		
BRDI	BRDI = [$R_{rs}(442.5) - R_{rs}(560)$] / $R_{rs}(490)$	1.5038	1.1116	-0.6987	-1.1111	1.1555	-0.2960
<i>Final hybrid algorithm weighting between POC_{MBR} and POC_{BRDI}</i>							
If BRDI < 1 then	POC = POC _{MBR}						
If BRDI ≥ 1 then	POC = POC _{MBR} W _{MBR} + POC _{BRDI} W _{BRDI} where W _{MBR} = 0.5[W _{MBR} + (1 - w _{BRDI})] and W _{BRDI} = 1 - W _{MBR}						
<i>Calculation of weighting factors w_{MBR} and w_{BRDI}</i>							
If POC _{MBR} > 25 mg m ⁻³ then w _{MBR} = 1							
If 15 ≤ POC _{MBR} ≤ 25 mg m ⁻³ then w _{MBR} = log[0.9 POC _{MBR} - 12.5]							
If POC _{MBR} < 15 mg m ⁻³ then w _{MBR} = 0							
If POC _{BRDI} > 25 mg m ⁻³ then w _{BRDI} = 0							
If 15 ≤ POC _{BRDI} ≤ 25 mg m ⁻³ then w _{BRDI} = 1 - log[0.9 POC _{BRDI} - 12.5]							
If POC _{BRDI} < 15 mg m ⁻³ then w _{BRDI} = 1							

^a MBR-based OC3 and OC4 algorithms: $\log(\text{POC}) = a_0 + a_1 \log(\text{MBR}) + a_2 [\log(\text{MBR})]^2 + a_3 [\log(\text{MBR})]^3$.

^b BRDI algorithm: $\log(\text{POC}) = a_0 + a_1 \text{BRDI} + a_2 \text{BRDI}^2 + a_3 \text{BRDI}^3 + a_4 \text{BRDI}^4 + a_5 \text{BRDI}^5$.

^c One variant of hybrid algorithm consists of MBR-OC3 and BRDI and the other variant consists of MBR-OC4v and BRDI.

^d the letter “v” indicates use of a calculated virtual band in the algorithm.

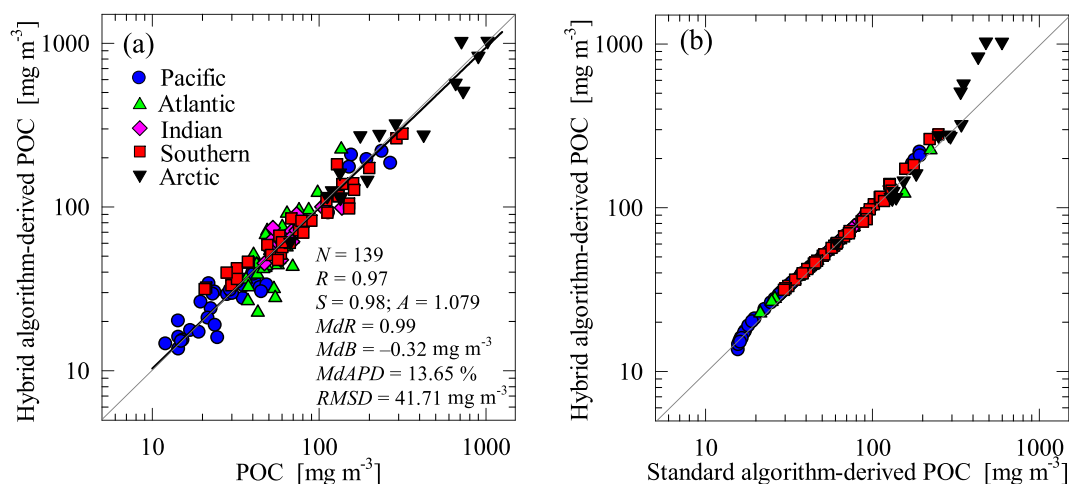


Fig. 10. (a) The SeaWiFS hybrid algorithm-derived POC vs. measured POC for the POC algorithm development dataset. A model-II regression line fit to the log-transformed data (black solid line) and the 1:1 line (thin grey line) are shown along with several statistical parameters. (b) A comparison of the SeaWiFS hybrid algorithm-derived POC and POC derived from the current standard algorithm used by NASA OBPB for the algorithm development dataset. The thin grey line is a 1:1 line. The data from different oceanic basins are depicted as indicated in panel (a).

this initial condition is to avoid using the weighting approach for hypothetical (but rather unlikely) scenario when $POC_{BRDI} > 45 \text{ mg m}^{-3}$ and $POC_{MBR} < 25 \text{ mg m}^{-3}$.

Fig. 10a encapsulates the formulation of SeaWiFS-specific hybrid algorithm by comparing POC derived from the hybrid algorithm with measured POC for our entire development dataset. The statistical parameters of this relationship indicate that overall the hybrid algorithm describes well the observations, for example $S = 0.98$, $MdR = 0.99$, $MdAPD = 13.6\%$, and $RMSD = 41.7 \text{ mg m}^{-3}$. The statistical parameters of the hybrid algorithm are similar or slightly better compared with the cases illustrated in Figs. 7 and 8 where the MBR-OC4 or the MBRDI algorithm alone were used over the entire dynamic range of POC. When compared with the current standard algorithm based on BR-PF formula, the new hybrid algorithm is expected to produce lower values at the low end (i.e., ultraoligotrophic waters) and higher values at the high end (e.g., highly eutrophic waters) of the POC range (Fig. 10b). These features are considered as main improvements over the current standard algorithm. Over a significant range of intermediate values of POC the new hybrid algorithm is, however, expected to produce similar results to the current standard algorithm. These results are consistent with the behavior of the best-fit functions of BR-PF, MBR-OC4, and BRDI in Figs. 6, 7, and 9.

Table 4 provides essential information for the final POC algorithms for SeaWiFS as well as MODIS, VIIRS, MERIS, and OLCI satellite sensors. The MERIS and OLCI sensors have spectral bands in the blue and green regions which are centered at wavelengths similar to SeaWiFS, specifically 442.5, 490, 510, and 560 nm [note that in our algorithm development dataset $R_{rs}(442.5)$ was calculated by averaging $R_{rs}(442)$ and $R_{rs}(443)$]. Therefore, for MERIS and OLCI we formulated the sensor-specific hybrid algorithms that combine the component MBR-OC4 and BRDI algorithms in a similar fashion as for SeaWiFS. The statistical indicators of goodness-of-fit for these algorithms are similar to those displayed in Fig. 10a for SeaWiFS (Table S4, Supplementary Material).

The MODIS and VIIRS sensors lack a band centered at or near 510 nm. For these sensors we formulated two variants of hybrid algorithms and both variants are shown in Table 4. The first variant is based on the use of three bands from the blue-green region which are available on these sensors, specifically 443, 488, and 547 nm for MODIS, 443, 486, and 551 nm for VIIRS-SNPP, and 445, 489, and 556 nm for VIIRS-JPSS-1. This variant of MODIS and VIIRS-specific hybrid algorithms combine the MBR and BRDI formulas in a similar fashion as SeaWiFS with the

exception that MBR-OC3 formula is used instead of MBR-OC4. In the MBR-OC3 formulas the maximum band ratio is selected from two band ratios, i.e., $R_{rs}(443)/R_{rs}(547)$ and $R_{rs}(488)/R_{rs}(547)$ for MODIS, $R_{rs}(443)/R_{rs}(551)$ and $R_{rs}(486)/R_{rs}(551)$ for VIIRS-SNPP, and $R_{rs}(445)/R_{rs}(556)$ and $R_{rs}(489)/R_{rs}(556)$ for VIIRS-JPSS-1. The goodness-of-fit statistics of hybrid algorithms involving MBR-OC3 are somewhat inferior compared with the SeaWiFS hybrid algorithm involving MBR-OC4 (Table S4, Supplementary Material). This result is attributable to the algorithm predictions in the range of relatively high POC where the MBR-OC4 formula uses the third band ratio that includes 510 nm, i.e., $R_{rs}(510)/R_{rs}(555)$ in the case of SeaWiFS. Specifically, the MBR-OC3 tends to underestimate the POC measurements in our development dataset at the high end of POC range. This observation motivated a development of a second variant of MODIS and VIIRS-specific hybrid algorithms.

In this second variant of MODIS and VIIRS algorithms the MBR-OC4v formula is used, in which $R_{rs}(510v)$ is estimated from reflectances measured by MODIS and VIIRS at other bands. We note that the BRDI component of these hybrid algorithms is the same as in the first variant of hybrid algorithms. We here use “510v” to indicate that this is a “virtual” band centered at 510 nm rather than a band at which the measurement is actually made, and also “MBR-OC4v” to indicate the use of this virtual band in the MBR-OC4 algorithm. For MODIS $R_{rs}(510v)$ is estimated from measurements of $R_{rs}(488)$ and $R_{rs}(531)$. This makes it possible to include the third band ratio, $R_{rs}(510v)/R_{rs}(547)$, in the MODIS MBR-OC4v algorithm. For VIIRS-SNPP the estimation of $R_{rs}(510v)$ uses the measurements of $R_{rs}(486)$ and $R_{rs}(551)$, and for VIIRS-JPSS-1 the measurements of $R_{rs}(489)$ and $R_{rs}(556)$ are used. These estimations of $R_{rs}(510v)$ allow the formulation of VIIRS MBR-OC4v algorithms. Because the approach to formulate the MBR-OC4v algorithms is essentially the same for MODIS and VIIRS sensors except for differences in center wavelengths of bands, we limit the relevant description to MODIS.

Fig. 11a illustrates the MODIS-specific MBR-OC4 algorithm as fitted to our development dataset assuming hypothetically that MODIS is equipped with a 510-nm band. The data in Fig. 11a are color coded to distinguish the measured reflectance ratios selected as maximum band ratios that provide input to the MBR-OC4 formula. As seen, $R_{rs}(510)/R_{rs}(547)$ can be selected as the MBR value only when POC is relatively high ($> 100 \text{ mg m}^{-3}$), which corresponds to the range of MBR values less than about 1.2. Note also that the MBR range between about 1 to 1.2

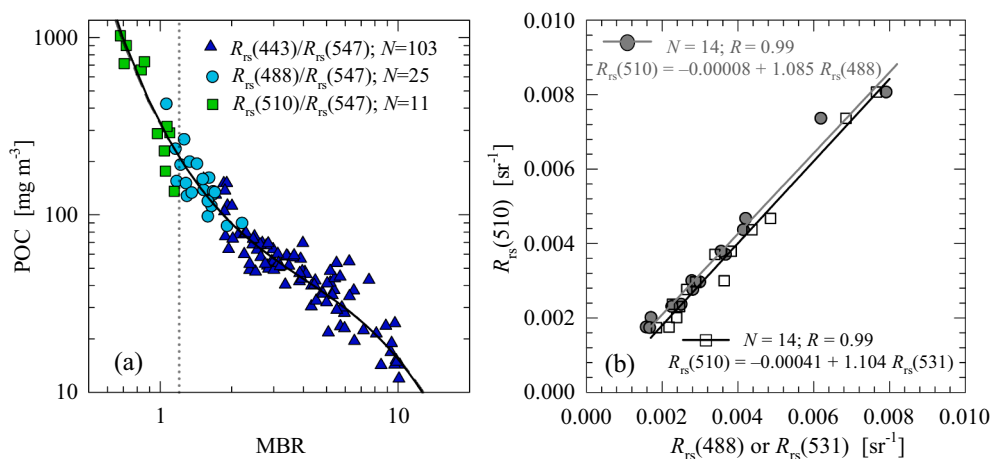


Fig. 11. (a) POC as a function of MBR (Maximum Band Ratio) for the POC algorithm development dataset. The three band ratios of $R_{rs}(\lambda)$ considered in this analysis are indicated. The 443, 488, and 547 nm bands are available on the MODIS instrument, but the 510 nm band is not available. Different data symbols are used to indicate which band ratio has the maximum value for any given data point. The best-fit cubic polynomial function to the data is shown (solid line). Also, the best-fit function (dashed line) is shown for the same dataset but with $R_{rs}(510)/R_{rs}(547)$ replaced with $R_{rs}(510v)/R_{rs}(547)$ where $R_{rs}(510v)$, referred to as R_{rs} at the virtual band of 510 nm, is estimated from $R_{rs}(488)$ and $R_{rs}(531)$. The best-fit dashed line is virtually indistinguishable from the best-fit solid line. The vertical dotted line at $MBR = 1.2$ indicates the upper limit of the range of MBR values within which $R_{rs}(510v)$ is used in the MODIS hybrid algorithm (see text in Section 6 for details). (b) $R_{rs}(510)$ as a function of $R_{rs}(488)$ or $R_{rs}(531)$ for the subset of data from the POC algorithm development dataset which satisfies a condition $MBR < 1.2$. Two relationships which serve as a basis for estimation of $R_{rs}(510v)$ are shown; one between $R_{rs}(510)$ and $R_{rs}(488)$ and the other between $R_{rs}(510)$ and $R_{rs}(531)$. The ordinary least squares regression rather than the robust regression method was used to determine the relationships for estimating $R_{rs}(510v)$ because the use of equal weights was deemed preferable for this number and distribution of data points (differences between the two methods were nevertheless very small).

represents an overlap range where either $R_{rs}(510)/R_{rs}(547)$ or $R_{rs}(488)/R_{rs}(547)$ is selected as the MBR value. These results indicate that a subset of our measurements satisfying the condition $MBR < 1.2$ is best suited to test the estimation of $R_{rs}(510v)$ from R_{rs} measured at other wavelengths available on MODIS, specifically from $R_{rs}(488)$ and $R_{rs}(531)$. This subset of data includes 9 measurements from the Arctic Ocean, 2 measurements from the Southern Ocean, 2 measurements from the Pacific Ocean, and 1 measurement from the Atlantic Ocean.

Such estimation is supported in Fig. 11b which shows a very strong correlation ($R = 0.99$) between the measured $R_{rs}(510)$ and $R_{rs}(488)$ or $R_{rs}(531)$. The linear functions obtained from a model-I regression are also shown and provide a means to estimate $R_{rs}(510v)$. Although the agreement between the estimated $R_{rs}(510v)$ and measured $R_{rs}(510)$ is very good regardless of whether $R_{rs}(488)$ or $R_{rs}(531)$ is used, we have chosen to use an average estimate of $R_{rs}(510v)$ based on the two linear regression functions shown in Fig. 11b.

An important result shown in Fig. 11a is that the curve representing the MBR-OC4v formula involving the use of the estimated $R_{rs}(510v)$ is essentially indistinguishable from the curve in which the MBR-OC4 formula uses the actual measured $R_{rs}(510)$. The agreement between the two curves, especially in the range of $MBR < 1.2$ within which $R_{rs}(510v)$ is intended for use, reflects the good estimation of $R_{rs}(510v)$ as illustrated in Fig. 11b.

The best-fit coefficients of the MODIS-specific hybrid algorithm combining the MBR-OC4v and BRDI components are presented in Table 4 along with a description of formulas for estimating $R_{rs}(510v)$ from $R_{rs}(488)$ or $R_{rs}(531)$. For operational use this MODIS hybrid algorithm is also subject to an initial condition which implies that $R_{rs}(510v)/R_{rs}(547)$ is used in the MBR-OC4v formula only when the value of $R_{rs}(510v)/R_{rs}(547)$ is less than 1.2 and is greater than the values of $R_{rs}(443)/R_{rs}(547)$ and $R_{rs}(488)/R_{rs}(547)$ (Table 4). Note that field data (Fig. 11a) demonstrate that $R_{rs}(488)/R_{rs}(547)$ can be the highest band ratio below the threshold of 1.2, so this threshold does not act as an automatic or abrupt switch between the use of $R_{rs}(510v)/R_{rs}(547)$ or $R_{rs}(488)/R_{rs}(547)$ in the MBR-OC4v formula. It is also important to note that the statistical indicators of the goodness-of-fit of this MODIS hybrid algorithm for our development dataset (e.g., $S = 0.97$, $MdR = 1.01$, $MdAPD = 14.5\%$, and $RMSD = 44.9 \text{ mg m}^{-3}$) are very close to those displayed in Fig. 10a for the SeaWiFS hybrid algorithm (see also Table

S4, Supplementary Material). This result indicates a high degree of consistency of the MODIS and SeaWiFS hybrid algorithms and supports the notion that the MODIS hybrid algorithm based on MBR-OC4v and BRDI is preferable over the other variant of the MODIS algorithm based on MBR-OC3 and BRDI (Table S4). We recall that the BRDI component is the same for these two variants of MODIS hybrid algorithms.

A similar conclusion and results follow from analogous analysis of two variants of the VIIRS hybrid algorithms for both VIIRS-SNPP and VIIRS-JPSS-1 sensors. One notable distinction is the estimation of $R_{rs}(510v)$ which for VIIRS sensors is somewhat degraded compared to MODIS. This is because the VIIRS bands used to estimate $R_{rs}(510v)$ are generally further away from 510 nm compared to the MODIS case. As a result, the relationships for estimating $R_{rs}(510v)$ are slightly weaker although the correlation coefficients for these relationships remain very high, for example $R = 0.99$ and 0.95 for estimation of $R_{rs}(510v)$ from the VIIRS-SNPP bands of 486 nm and 551 nm, respectively. In addition to the best-fit coefficients of VIIRS algorithms, Table 4 also provides equations for the estimation of $R_{rs}(510v)$ from the VIIRS measurements at the blue and green bands. These equations indicate a stronger contribution of the blue band than the green band in the estimation of $R_{rs}(510v)$ which results from the spectral distance between 510 nm and the two other wavelengths. Like for MODIS, our analysis of the development dataset suggests that for the VIIRS sensors the variant of the hybrid algorithm combining MBR-OC4v and BRDI is preferable over the other variant combining MBR-OC3 and BRDI (Table S4, Supplementary Material).

7. Example validation and application of POC algorithms with satellite imagery

A thorough validation of proposed POC algorithms and their comparison with several existing POC algorithms using independent field data as well as in situ-satellite matchup datasets warrants a separate study which is underway. Here we present example validation results for the proposed SeaWiFS and MODIS hybrid algorithms and comparison with the current standard algorithms used by NASA OBPB for generating the global POC product from these satellite sensors (Fig. 12). These comparisons are based on a matchup dataset of satellite-derived $R_{rs}(\lambda)$ and field measurements of POC, which has been used by NASA OBPB for

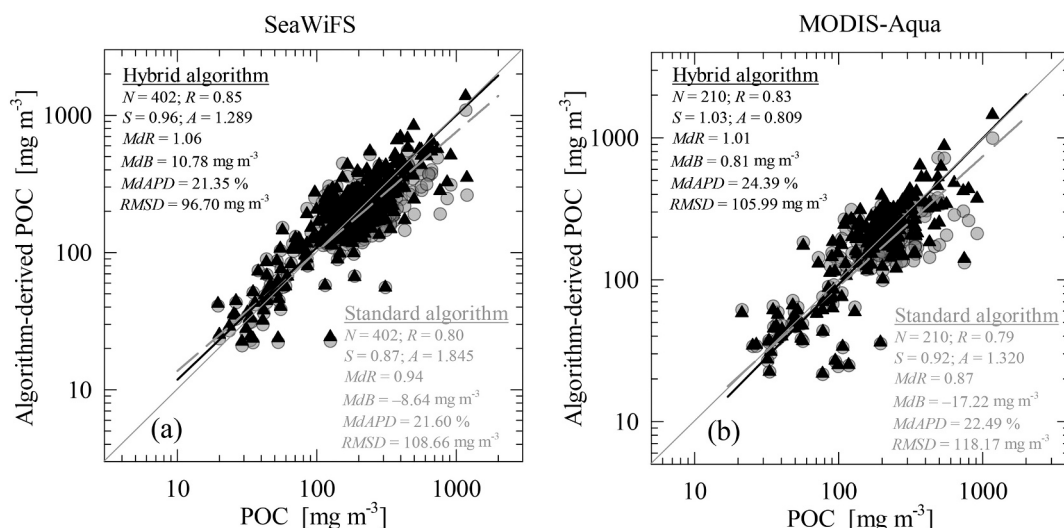


Fig. 12. A comparison of algorithm-derived POC (the vertical axis) with measured POC (the horizontal axis) for a matchup dataset of in situ and satellite observations with (a) SeaWiFS and (b) MODIS-Aqua. (a) Validation of SeaWiFS-specific hybrid POC algorithm (black triangles) and current standard POC algorithm used by NASA OBPB for SeaWiFS observations (grey circles). (b) Same as (a) but for MODIS-Aqua. Model II regression lines fit to log-transformed data of the hybrid algorithm-derived POC vs. measured POC (black solid lines) and the standard algorithm-derived POC vs. measured POC (dashed grey lines) are shown. The thin grey solid line is a 1:1 line. Several statistical parameters are displayed for this comparative data analysis.

demonstrating the performance of standard POC algorithms with SeaWiFS and MODIS-Aqua observations (<https://oceancolor.gsfc.nasa.gov/atbd/poc/>). The validation dataset for SeaWiFS consists of 402 observations, most of them (350) collected in the Atlantic along the east coast of the United States. The remaining observations were made at low to temperate latitudes in the Atlantic (22) and Pacific (29), and only one observation was made at high latitudes in the north polar Atlantic. In this dataset the surface values of POC obtained from field measurements range from about 20 to 1190 mg m^{-3} but the probability distribution peaks near 200 mg m^{-3} . This indicates a significant shift towards higher values of POC compared to distributions for our algorithm development dataset and global satellite data (see Fig. 3). The MODIS-Aqua validation dataset consists of 210 observations, also with most observations (154) collected along the east coast of the United States. The remaining data come from high northern latitudes (8 in the Chukchi Sea and one in the north polar Atlantic) and low to temperate latitudes in the Atlantic (28), Pacific (15), as well as a few observations south of South Africa and Tasmania. The surface POC in this dataset ranges from about 21 to 1170 mg m^{-3} with a probability distribution peaking at about 200 mg m^{-3} , which is similar to the SeaWiFS validation dataset.

Fig. 12 demonstrates that the statistical parameters of the relationship between the satellite-derived POC and measured POC are generally better for the hybrid algorithm than the standard algorithm for both the SeaWiFS and MODIS-Aqua matchup datasets. In particular, the parameters S and A are much closer to 1 for the hybrid algorithms indicating that the best-fit regression functions for these matchup datasets are closer to the 1:1 line when the hybrid algorithm is used (black solid lines in Fig. 12) compared with the use of the standard algorithm (grey dashed lines). Although these matchup datasets include a relatively small proportion of data from low POC waters, these results point to potential improvements provided by the hybrid algorithms. Specifically, the SeaWiFS and MODIS-derived POC obtained with standard algorithms tend to be lower than the measured values within the range of high POC above a few hundred mg m^{-3} . This tendency for underestimation is not seen for the hybrid algorithms. Within the intermediate range of POC around 100 mg m^{-3} both types of algorithms yield similar

results. This result is consistent with the differences between the hybrid and standard algorithms for our algorithm development dataset as depicted in Fig. 10b. In addition, Fig. 12 shows that the use of hybrid algorithms with satellite data of $R_{rs}(\lambda)$ tends to provide somewhat lower POC values than the standard algorithms at very low POC. This result is also consistent with the behavior of these algorithms for the development dataset (Figs. 6–9) and is expected to be an improvement associated with the use of BRDI in the hybrid algorithm at very low POC.

Example monthly composite images of POC obtained with the hybrid algorithm applied to SeaWiFS observations are illustrated in Fig. 13. The images of the difference between POC derived from the hybrid and current standard algorithms are also shown. Vast areas of subtropical ocean exhibit small positive differences, typically a few mg m^{-3} . Certain areas at tropical, subtropical, or temperate latitudes show some negative difference, for example the ultraoligotrophic waters within the central part of the South Pacific Gyre in the January 2005 image which is associated with the use of the BRDI component of the hybrid algorithm in this particular situation. Significant positive difference is typically observed in waters with high POC as clearly seen at northern latitudes in the July 2005 image or various coastal/shelf areas and upwelling regions along the western continental boundaries. Again, this is consistent with expectations based on differences in the algorithm behavior for the algorithm development dataset.

Fig. 14a compares POC derived from hybrid algorithms using SeaWiFS and MODIS-Aqua observations of the global ocean in the month of July 2005, and Fig. 14b shows similar comparison for MODIS-Aqua and VIIRS-SNPP for January 2017. The majority of data points in these plots are clustered along the 1:1 line indicating good agreement, on average, between the satellite retrievals of POC from different sensors. In addition, the overall pattern of scattered points does not exhibit a bias over a wide dynamic range of derived values of POC. Although comparative analysis of POC derived from different satellite sensors requires special attention in further studies, the example results presented in Fig. 14 are promising indicators of consistency of long-term record of global POC product based on the proposed hybrid algorithms as applied to multiple satellite missions.

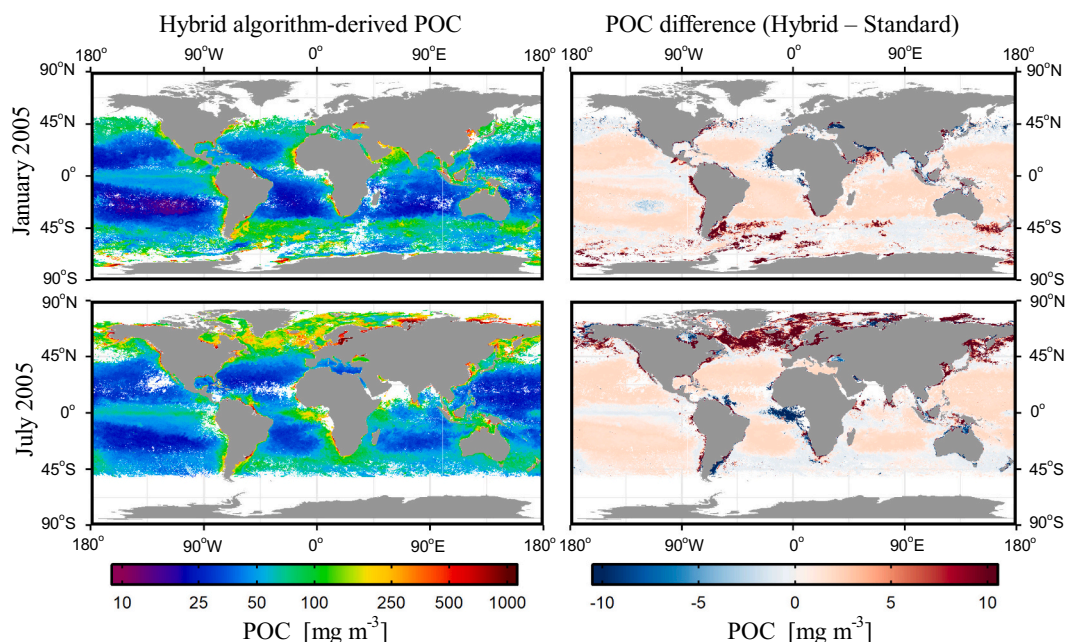


Fig. 13. (Left panels) Monthly composite images of POC in surface waters of the global ocean derived from the SeaWiFS-specific hybrid algorithm applied to SeaWiFS observations during two example months, January 2005 and July 2005. (Right panels) The corresponding global images of the difference between POC values derived from the hybrid algorithm and the current standard algorithm used by NASA OBPG.

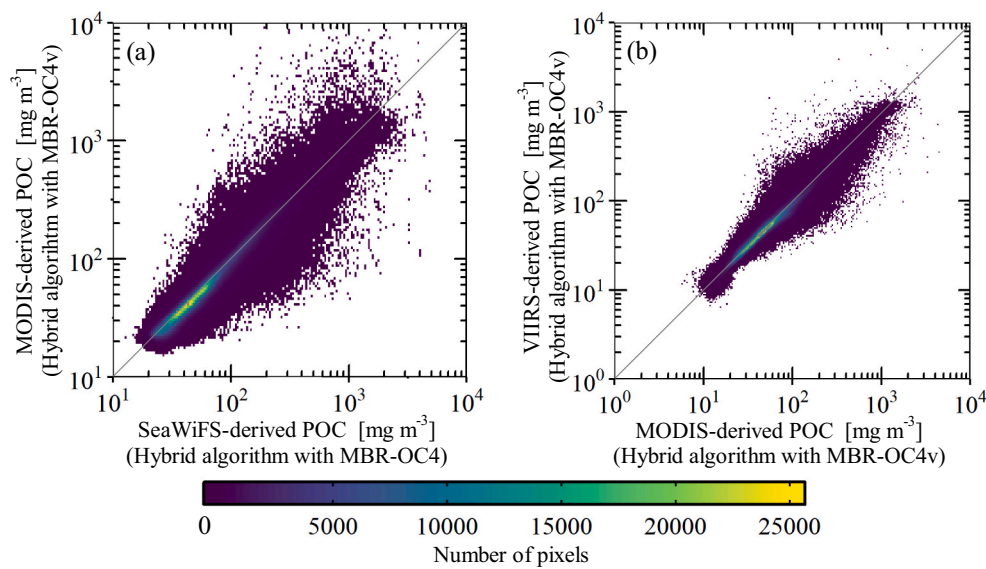


Fig. 14. (a) A comparison of POC derived from SeaWiFS-specific and MODIS-specific hybrid algorithms using global monthly composite data from SeaWiFS and MODIS-Aqua observations in July 2005. (b) A comparison of POC derived from MODIS-specific and VIIRS-specific hybrid algorithms using global monthly composite data from MODIS-Aqua and VIIRS-SNPP observations in January 2017.

8. Summary and future perspectives

Chlorophyll-a concentration in water has been a cornerstone data product of optical remote sensing since the first space-based ocean color mission of Coastal Zone Color Scanner (CZCS) on Nimbus-7 satellite launched in 1978 (Hovis et al., 1980). The use of empirical Chla algorithms that are based on multi-spectral measurements of ocean reflectance from space span more than four decades (Gordon and Clark, 1980; Morel, 1980). Over the years multiple refinements of global empirical Chla algorithms have been formulated to meet the goals of the development of Chla climate data record from satellite ocean color missions (Hu et al., 2012; O'Reilly et al., 1998; O'Reilly et al., 2000; O'Reilly and Werdell, 2019). Although it is carbon, not chlorophyll-a, which is of more direct relevance to the ocean's role in the Earth's carbon cycle, the development of algorithms for estimating ocean carbon pools has a much shorter history than Chla. The first POC algorithm was proposed during early years of SeaWiFS ocean color mission (Stramski et al., 1999) and, until now, essentially one version of an empirical POC algorithm based on the power function of the blue-green reflectance ratio (Stramski et al., 2008) has been used by NASA for routine determinations of global POC product from past and current satellite ocean color missions. In the present study we generated a new suite of global empirical POC algorithms for past and current satellite sensors to support development of a long-term POC data record from multiple satellite missions.

For this development we assembled a field dataset of concurrent POC and remote-sensing reflectance, $R_{rs}(\lambda)$, measurements. Although the size of this development dataset is not very large ($N = 139$), the data were collected in all major ocean basins encompassing tropical, subtropical, and temperate latitudes as well as the northern and southern polar latitudes, which yielded a globally-representative probability distribution of POC with a broad range of values between about 10 and 1000 mg m^{-3} (Table 1, Fig. 3). When creating the development dataset, we also applied additional inclusion and exclusion criteria based on well-assured and documented consistency of measurement protocols as well as specific bio-optical and particle characteristics of seawater which are consistent with vast areas of open-ocean pelagic environments. To formulate the algorithms the dataset was subject to parametric regression analysis. Overall we evaluated over seventy formulas for estimating POC from $R_{rs}(\lambda)$ using seven distinctly different algorithmic categories.

The key difference between these categories is associated with fundamentally different definitions of independent (or explanatory) variable of $R_{rs}(\lambda)$ in the algorithm formulas.

As a result of goodness-of-fit analysis, we selected the best candidate POC algorithms for SeaWiFS, MODIS, VIIRS, MERIS, and OLCI satellite sensors (Table 4). These best candidates are referred to as hybrid algorithms and consist of two components, the MBR-OC4 cubic polynomial function and BRDI quintic polynomial function. The MBR-OC4 is the Maximum Band Ratio algorithm with four spectral bands, for example 443, 490, 510, and 555 nm for SeaWiFS. For MODIS and VIIRS sensors the measurements at 510 nm are not available and we use $R_{rs}(510v)$ that represents the estimates of reflectance at 510 nm from measurements at other bands available on these sensors (Fig. 11, Table 4). The BRDI is the Band Ratio Difference Index which involves three spectral bands, for example 443, 490, and 555 nm for SeaWiFS. The MBR-OC4 algorithm is used for POC > 25 mg m^{-3} and the BRDI for POC < 15 mg m^{-3} . In the transition region the final POC value is calculated by applying a weighting approach to POC estimates obtained from MBR-OC4 and BRDI formulas. The main role of the BRDI component of the hybrid algorithm is to improve estimation of very low POC in ultraoligotrophic waters. The MBR-OC4 component aims at improving the POC estimates compared with the current standard algorithm over a broader range of POC values, but especially for relatively high POC above a few hundred mg m^{-3} . A preliminary analysis of field-satellite matchup datasets based on SeaWiFS and MODIS-Aqua observations showed improved performance of hybrid algorithms compared with current standard algorithms for both SeaWiFS and MODIS. We also demonstrated a reasonable consistency between POC derived from hybrid algorithms applied to SeaWiFS, MODIS-Aqua, and VIIRS-SNPP satellite imagery.

As field determinations of POC play an important role in satellite algorithm development and validation, it is important to acknowledge that the common method based on POC determinations of particulate matter collected on glass-fiber filters is subject to various sources of uncertainties. A recently published protocol document provides a detailed discussion of various aspects of methodology for measuring POC in seawater, including recommendations for standardized practices to determine POC retainable on filters (IOCCG Protocol Series, 2021). The quantification of missing POC (mainly colloidal matter from sub-micrometer size range) with the standard filtration-based methodology remains, however, unresolved. As briefly discussed in Section 3.2, the

colloidal POC can be important from the standpoint of both the total POC in seawater and the ocean optical properties, and hence the optically-based POC algorithms. In this study, we draw particular attention to two opposite biasing effects of the current POC measurement methodology; DOC-adsorption which results in positive bias of POC retained by GF/F filters and incomplete retention of all POC-bearing particles by GF/F filters which results in negative bias relative to total POC in seawater. Our algorithm development dataset includes POC determinations obtained with the JGOFS protocol established in the 1990s. This protocol involves no correction for DOC-adsorption, so it does not necessarily aim at optimizing the determination of the specific fraction of total POC which is retained by the GF/F filters. However, it is conceivable that the JGOFS protocol can provide POC data that more closely approximate the total POC in seawater compared to what would be obtained with an alternative protocol involving the correction for DOC-adsorption. This is because the opposite biasing effects of DOC-adsorption and the missing portion of total POC may be similar in relative magnitude and thus largely counteract each other. For studies of ocean biogeochemistry and optical remote sensing of POC, a measure of total POC in seawater is more relevant than a strictly operational measure of POC fraction retained on GF/F filters. In particular, the remote-sensing reflectance is sensitive to all suspended particles including very small particles unaccounted for by the collection of particulate matter on GF/F filters. Thus, although the POC protocol without correction for DOC adsorption does not represent a perfect methodological approach for measuring the total POC in seawater, it does have potential advantages within the broader context of applications to ocean optical remote sensing and biogeochemistry. For these reasons it appears that the continued use of POC algorithms based on POC measurements without correction for DOC adsorption, as proposed here through a new suite of sensor-specific algorithms in Table 4, remains warranted. This is also consistent with the current standard algorithms for generating the global POC product. However, it is still highly desirable to improve the POC measurement methodology in the future, so it will more accurately represent the total POC in seawater, especially by including the small-sized particulate fraction that is missed by the current standard methodology. When such future improvements in methodology are developed, the POC data product obtained from algorithms such as those in Table 4 will have an important historical benchmarking value.

The POC measurement protocol involving the correction for DOC adsorption has the methodological benefit of standardizing the methodology that aims at optimizing the determination of POC which is

operationally defined as a fraction of total POC retainable by GF/F filters. Although this protocol has been increasingly used in recent years, the currently available data of concurrent measurements of $R_{rs}(\lambda)$ and POC corrected for DOC adsorption are insufficient to create a globally-representative dataset for development of global POC algorithms. Nevertheless, we conducted the analysis in which the POC measurements from our algorithm development dataset were retroactively corrected for DOC adsorption using a single relationship between the correction and the volume of filtered sample as proposed by Novak et al. (2018). While we recognize that such retroactive correction is subject to larger uncertainty compared with more rigorous sample-specific corrections executed during the acquisition of measurements, the formulation of preliminary algorithms using our dataset with retroactively DOC-corrected values of POC may have significant value, for example as baseline information for future work on POC algorithms, especially as standardized POC protocols are broadly implemented (IOCCG Protocol Series, 2021) and potential improvements in POC measurement methodology are developed to better account for colloidal POC.

Table 5 provides a summary of sensor-specific algorithm formulas obtained from our development dataset but with the use of DOC-corrected values of POC. The formulas shown in Table 5 were determined in the same fashion as the algorithmic formulas for the original (i.e., DOC-uncorrected) values of POC shown in Table 4. The only difference is that the main set of algorithms involving the original POC measurements (Table 4) is based on the entire algorithm development dataset ($N = 139$, Table 1) whereas the algorithmic formulas involving the DOC-corrected POC (Table 5) are based on a subset of these data for which sample filtration volumes were known ($N = 107$, see Section 3.2). Table S5 (Supplementary Material) provides the goodness-of-fit statistical parameters for all final hybrid algorithms presented in Table 5.

The main purpose of the new suite of empirical POC algorithms presented in this study is to provide an improved tool for the development of a global multi-decadal data record of POC in the surface ocean by merging observations from multiple satellite ocean color missions. In particular, the suite of algorithms presented in Table 4 can be viewed as the potential next generation version of POC global algorithms that offer a capability to generate a long-term sensor-to-sensor consistent data record of POC that begins with the launch of SeaWiFS in 1997. The next research task is to conduct a thorough validation analysis of the proposed algorithms and other algorithms available in literature with independent in situ and in situ-satellite matchup datasets.

Table 5

Final hybrid algorithm formulations and parameter values based on the algorithm development dataset with DOC-corrected POC ($N = 107$). The weighting approach for hybrid algorithms and the use of virtual band (510v) is the same as described for algorithms presented in Table 4.

Algorithm	Reflectance band parameter	a_0	a_1	a_2	a_3	a_4	a_5
<i>SeaWiFS hybrid algorithm</i>							
MBR-OC4	$MBR = \max[R_{rs}(443, 490, 510)/R_{rs}(555)]$	2.4644	-2.2866	2.1514	-1.1324		
BRDI	$BRDI = [R_{rs}(443) - R_{rs}(555)] / R_{rs}(490)$	3.4782	-8.1773	15.4520	-14.7159	6.7378	-1.1942
<i>MODIS hybrid algorithm</i>							
MBR-OC3	$MBR = \max[R_{rs}(443, 488)/R_{rs}(547)]$	2.4090	-2.2423	2.1074	-1.1821		
MBR-OC4v	$MBR = \max[R_{rs}(443, 488, 510v)/R_{rs}(547)]$	2.4792	-2.8271	3.3208	-1.8951		
BRDI	$BRDI = [R_{rs}(443) - R_{rs}(547)] / R_{rs}(488)$	2.9821	-6.3986	13.3257	-14.0553	7.0613	-1.3653
<i>VIIRS-SNPP hybrid algorithm</i>							
MBR-OC3	$MBR = \max[R_{rs}(443, 486)/R_{rs}(551)]$	2.4066	-2.0500	1.7259	-0.9300		
MBR-OC4v	$MBR = \max[R_{rs}(443, 486, 510v)/R_{rs}(551)]$	2.4920	-2.7393	3.1073	-1.7160		
BRDI	$BRDI = [R_{rs}(443) - R_{rs}(551)] / R_{rs}(486)$	3.8829	-11.1351	23.0733	-23.7939	11.7839	-2.2599
<i>VIIRS-JPSS-1 hybrid algorithm</i>							
MBR-OC3	$MBR = \max[R_{rs}(445, 489)/R_{rs}(556)]$	2.4230	-1.9173	1.4426	-0.7664		
MBR-OC4v	$MBR = \max[R_{rs}(445, 489, 510v)/R_{rs}(556)]$	2.4890	-2.4459	2.4857	-1.3480		
BRDI	$BRDI = [R_{rs}(445) - R_{rs}(556)] / R_{rs}(489)$	4.5702	-14.2259	28.4159	-28.0756	13.3419	-2.4556
<i>MERIS and OLCI hybrid algorithms</i>							
MBR-OC4	$MBR = \max[R_{rs}(442.5, 490, 510)/R_{rs}(560)]$	2.4606	-2.0561	1.7281	-0.8859		
BRDI	$BRDI = [R_{rs}(442.5) - R_{rs}(560)] / R_{rs}(490)$	3.8522	-9.6080	17.5368	-16.0773	7.1088	-1.2191

Credit author statement

Conception and design of study: DS, IJ, RAR.
 Methodology: DS, IJ, RAR.
 Data acquisition and curation: RAR, DS, IJ.
 Formal data analysis: IJ, DS, RAR.
 Writing original draft: DS.
 Revising the manuscript: DS, IJ, RAR.
 Approval of the manuscript: DS, IJ, RAR.

Declaration of Competing Interest

Dariusz Stramski reports financial support was provided by NASA. Ishan Joshi reports financial support was provided by NASA. Rick A. Reynolds reports financial support was provided by NASA.

Acknowledgments

This work was supported by the National Aeronautics and Space Administration [Grant 80NSSC18K0956]. A major portion of field data used in this study was collected on eleven cruises (i.e., the Pacific, Atlantic, Southern Ocean AESOPS, and Arctic cruises) in which the members of our lab participated with previous NASA, NSF, and ONR support. We are grateful to the scientists, officers and crews on these cruises for assistance and support in fieldwork. Special thanks go to M. Babin, A. Bricaud, D. Doxaran, J. Ehn, A. Fujiwara, T. Hirawake, S. Hooker, M. Lewis, A. Matsuoka, G. Mitchell, R. Röttgers for sharing of data from these cruises. Some of these data, in particular the radiometric data, were obtained from the NASA SeaWiFS Bio-Optical Archive and Storage System (SeaBASS; <https://seabass.gsfc.nasa.gov/>) and French LEFE CYBER Database (http://www.obs-vlfr.fr/proof/vt/op/ec/biosop_e/bio.htm). We also thank the data providers for the three Arabian Sea cruises and the Southern Ocean AMLR2001 cruise. Data from the Arabian Sea were obtained from the U.S. JGOFS Data System (<http://us.jgofs.whoi.edu/jg/dir/jgofs/arabian/>) and data from AMLR2001 from SeaBASS. We also kindly thank the NASA Ocean Biology Processing Group for the production and distribution of the SeaWiFS, MODIS, and VIIRS imagery used in this study, and D. Robinson for assistance with satellite data processing. We express our appreciation to three anonymous reviewers for providing constructive comments on the manuscript.

Appendix A. Supplementary Material

Supplementary Material to this article can be found online at <https://doi.org/10.1016/j.rse.2021.112776>.

References

- Abdel-Moati, A.R., 1990. Adsorption of dissolved organic carbon (DOC) on glass fiber filters during particulate organic carbon (POC) determination. *Water Res.* 24, 763–764.
- Allison, D.B., Stramski, D., Mitchell, B.G., 2010a. Seasonal and interannual variability of particulate organic carbon within the Southern Ocean from satellite ocean color observations. *J. Geophys. Res.* 115, C06002. <https://doi.org/10.1029/2009jc005347>.
- Allison, D.B., Stramski, D., Mitchell, B.G., 2010b. Empirical ocean color algorithms for estimating particulate organic carbon in the Southern Ocean. *J. Geophys. Res.* 115, C10044. <https://doi.org/10.1029/2009jc006040>.
- Altman, D.G., Bland, J.M., 1983. Measurement in medicine: the analysis of method comparison studies. *Statistician* 32, 307–317.
- Antoine, D., Hooker, S.B., Belanger, S., Matsuoka, A., Babin, M., 2013. Apparent optical properties of the Canadian Beaufort Sea – Part 1: Observational overview and water column relationships. *Biogeosciences* 10, 4493–4509. <https://doi.org/10.5194/bg-10-4493-2013>.
- Arrigo, K.R., 2015. Impacts of climate on ecosystems and chemistry of the Arctic Pacific environment (ICESCAPE). *Deep-Sea Res. Part II* 118 (Part A), 1–6.
- Arthur, C.R., Rigler, F.H., 1967. A possible source of error in the ¹⁴C method of measuring primary production. *Limnol. Oceanogr.* 12, 121–124.
- Aurin, D., Mannino, A., Lary, D.J., 2018. Remote sensing of CDOM, CDOM spectral slope, and dissolved organic carbon in the global ocean. *Appl. Sci.* 8, 2687. <https://doi.org/10.3390/app8122687>.
- Balch, W.M., Drapeau, D.T., Fritz, J.J., 2000. Monsoonal forcing of calcification in the Arabian Sea. *Deep-Sea Res. Part II* 47, 1301–1337.
- Beaton, A.E., Tukey, W., J. W., 1974. The fitting of power series, meaning polynomials, illustrated on band-spectroscopic data. *Technometrics* 16 (2), 147–185.
- Behrenfeld, M.J., Boss, E.S., Siegel, D.A., Shea, D.M., 2005. Carbon-based ocean productivity and phytoplankton physiology from space. *Glob. Biogeochem. Cycles* 19, 1–14. <https://doi.org/10.1029/2004GB002299>.
- Behrenfeld, M.J., Hu, Y., Hostetler, C.A., Dall’Olmo, G., Rodier, S.D., Hair, J.W., Trepte, C.R., 2013. Space-based lidar measurements of global ocean carbon stocks. *Geophys. Res. Lett.* 40, 4355–4360. <https://doi.org/10.1002/grl.50816>.
- Bianchi, T.S., Lambert, C.D., Santschi, P.H., Guo, L.D., 1997. Sources and transport of land-derived particulate and dissolved organic matter in the Gulf of Mexico (Texas Shelf/Slope): the use of lignin-phenols and loliolides as biomarkers. *Org. Geochem.* 27, 65–78. [https://doi.org/10.1016/S0146-6380\(97\)00040-5](https://doi.org/10.1016/S0146-6380(97)00040-5).
- Bishop, J.K.B., Edmond, J.M., 1976. A new large volume filtration system for the sampling of oceanic particulate matter. *J. Mar. Res.* 34, 181–198.
- Bland, J.M., Altman, D.G., 1983. Statistical method for assessing agreement between two methods of clinical measurement. *Lancet* 327 (8476), 307–310.
- Brewin, R.J.W., Sathyendranath, S., Müller, D., Brockmann, C., Deschamps, P.-Y., Devred, E., Doerffer, R., Fomferra, N., Franz, B., Grant, M., Groom, S., Horseman, A., Hu, C., Krasemann, H., Lee, Z.P., Maritorena, S., Mélin, F., Peters, M., Platt, T., Regner, P., Smyth, T., Steinmetz, F., Swinton, J., Werdell, J., White III, G.N., 2015. The Ocean Colour Climate Change Initiative: III. A round-robin comparison on in-water bio-optical algorithms. *Remote Sens. Environ.* 162, 271–294.
- Bricaud, A., Babin, M., Claustre, H., Ras, J., Tièche, F., 2010. Light absorption properties and absorption budget of Southeast Pacific waters. *J. Geophys. Res. Oceans* 115 (C8), C08009.
- Campbell, J., Antoine, D., Armstrong, R., Arrigo, K., Balch, W., Barber, R., Behrenfeld, M., Bidigare, R., Bishop, J., Carr, M.-E., Esaias, W., Falkowski, P., Hoepffner, N., Iverson, R., Kiefer, D., Lohrenz, S., Marra, J., Morel, A., Ryan, J., Vederrikov, V., Waters, K., Yentsch, C., Yoder, J., 2002. Comparison of algorithms for estimating ocean primary production from surface chlorophyll, temperature, and irradiance. *Glob. Biogeochem. Cycles* 16, 1035. <https://doi.org/10.1029/2001GB001444>.
- CEOS, 2014. CEOS Strategy for Carbon Observations from Space. The Committee on Earth Observation Satellites (CEOS) Response to the Group on Earth Observations (GEO) Carbon Strategy. Printed in Japan by JAXA and I&A Corporation.
- Cetinić, I., Perry, M.J., Briggs, N.T., Kallin, E., D’Asaro, E.A., Lee, C.M., 2012. Particulate organic carbon and inherent optical properties during 2008 North Atlantic Bloom Experiment. *J. Geophys. Res.* 117, C06028. <https://doi.org/10.1029/2011JC007771>.
- Claustre, H., Sciandra, A., Vaulot, D., 2008. Introduction to the special section bio-optical and biogeochemical conditions in the South East Pacific in late 2004: the BIOSOPE program. *Biogeosciences* 5, 679–691.
- Collos, Y., Jauzein, C., Hately, E., 2014. Particulate carbon and nitrogen determinations in tracer studies: The neglected variables. *Appl. Radiat. Isot.* 94, 14–22.
- Deering, D.W., Rouse, J.W., Haas, R.H., Schell, J.A., 1975. Measuring “forage production” of grazing units from Landsat MSS data. In: *Proceedings of the 10th International Symposium on Remote Sensing of Environment Vol. II*, 1169–1178. ERIM, Ann Arbor, Michigan.
- Doney, S.C., Lima, I., Moore, J.K., Lindsay, K., Behrenfeld, M.J., Westberry, T.K., Mahowald, N., Glover, D.M., McGillicuddy, D.J., Takahashi, T., 2009. Skill metrics for confronting global upper ocean ecosystem-biogeochemistry models against field and remote sensing data. *J. Mar. Syst.* 76, 95–112.
- Doxaran, D., Ehn, J., Bélanger, S., Matsuoka, A., Hooker, S., Babin, M., 2012. Optical characterisation of suspended particles in the Mackenzie River plume (Canadian Arctic Ocean) and implications for ocean colour remote sensing. *Biogeosciences* 9, 3213–3229.
- Duforêt-Gaurier, L., Loisel, H., Dessailly, D., Nordkvist, K., Alvain, S., 2010. Estimates of particulate organic carbon over the euphotic depth from in situ measurements. Application to satellite data over the global ocean. *Deep-Sea Res. I Oceanogr. Res. Pap.* 57, 351–367. <https://doi.org/10.1016/j.dsr.2009.12.007>.
- Eppley, R.W., Peterson, B.J., 1979. Particulate organic matter flux and planktonic new production in the deep ocean. *Nature* 282, 677–680.
- Evers-King, H., Martínez-Vicente, V., Brewin, R.J., Dall’Olmo, G., Hickman, A.E., Jackson, T., Kostadinov, T.S., Krasemann, H., Loisel, H., Röttgers, R., Roy, S., Stramski, D., Thomalla, S., Platt, T., Sathyendranath, S., 2017. Validation and intercomparison of ocean color algorithms for estimating particulate organic carbon in the oceans. *Front. Mar. Sci.* 4, 251. <https://doi.org/10.3389/fmars.2017.00251>.
- Fenchel, T., 1988. Marine plankton food chains. *Annu. Rev. Ecol. Syst.* 19, 19–38.
- Fox, J., Weisberg, S., 2011. *An R Companion to Applied Regression*, Second edition. Sage, Thousand Oaks, California.
- Friedrichs, M.A.M., Carr, M.-E., Barber, R.T., Scardi, M., Antoine, D., Armstrong, R.A., Asanuma, I., Behrenfeld, M.J., Buitenhuis, E.T., Chai, F., Christian, J.R., Ciotti, A.M., Doney, S.C., Dowell, M., Dunne, J., Gentili, B., Gregg, W., Hoepffner, N., Ishizaka, J., Kameda, T., Lima, I., Marra, J., Mélin, F., Moore, J.K., Morel, A., O’Malley, R.T., O’Reilly, J., Saba, V.S., Schmelz, M., Smyth, T.J., Tjiputra, J., Waters, K., Westberry, T.K., Winguth, A., 2009. Assessing the uncertainties of model estimates of primary productivity in the tropical Pacific Ocean. *J. Mar. Syst.* 76, 113–133.
- Fritsch, F.N., Carlson, R.E., 1980. Monotone piecewise cubic interpolation. *SIAM J. Numer. Anal.* 17, 238–246.
- Gardner, W.D., 1977. Incomplete extraction of rapidly settling particles from water samplers. *Limnol. Oceanogr.* 22, 764–768.
- Gardner, W.D., Richardson, M.J., Carlson, C.A., Hansell, D., Mishonov, A.V., 2003. Determining true particulate organic carbon: bottles, pumps and methodologies. *Deep-Sea Res. II* 50, 655–674.

- Gardner, W.D., Mishonov, A.V., Richardson, M.J., 2006. Global POC concentrations from in-situ and satellite data. *Deep-Sea Res. II* 53, 718–740. <https://doi.org/10.1016/j.dsr2.2006.01.029>.
- Goldman, J.C., Dennett, M.R., 1985. Susceptibility of some marine phytoplankton species to cell breakage during filtration and post-filtration rinsing. *J. Exp. Mar. Biol. Ecol.* 86, 47–58.
- Gordon, H.R., Clark, D.K., 1980. Atmospheric effects in the remote sensing of phytoplankton pigments. *Bound.-Layer Meteorol.* 18, 299–313.
- Gundersen, J.S., Gardner, W.D., Richardson, M.J., Walsh, I.D., 1998. Effects of monsoons on the seasonal and spatial distributions of POC and chlorophyll in the Arabian Sea. *Deep-Sea Res. II* 45, 2103–2132.
- Hewes, C.D., Wieland, J., Mitchell, B.G., Kahru, M., Holm-Hansen, O., 2001. Phytoplankton and optical oceanography. In: Lipsky, J. (Ed.), *AMLR 2000/2001 Field Season Report Objectives, Accomplishments and Tentative Conclusions*, NOAA-TM-NMFS-SWFC-314. NOAA Southwest Fisheries Science Center, La Jolla, California, pp. 37–50.
- Hovis, W.A., Clark, D.K., Anderson, F., Austin, R.W., Wilson, W.H., Baker, E.T., Ball, D., Gordon, H.R., Mueller, J.L., El-Sayed, S.Z., Sturm, B., Wrigley, R.C., Yentsch, C.S., 1980. Nimbus-7 Coastal Zone Color Scanner: System description and initial imagery. *Science* 210 (4456), 60–63.
- Hu, C., Lee, Z., Franz, B.A., 2012. Chlorophyll *a* algorithms for oligotrophic oceans: A novel approach based on three-band reflectance difference. *J. Geophys. Res.* 117, 1–25.
- Hu, S.B., Cao, W.X., Wang, G.F., Xu, Z.T., Lin, J.F., Zhao, W.J., Yang, Y.Z., Zhou, W., Sun, Z.H., Yao, L.J., 2016. Comparison of MERIS, MODIS, SeaWiFS-derived particulate organic carbon, and in situ measurements in the South China Sea. *Int. J. Remote Sens.* 37, 1585–1600.
- Intergovernmental Oceanographic Commission, 1994. *Protocols for the Joint Global Ocean Flux Study (JGOFS) Core Measurements*. Intergovernmental Oceanographic Commission, Scientific Committee on Oceanic Research, Manuals and Guides No. 29. UNESCO-IOC, Paris, 170 pp.
- IOCCG Protocol Series, 2019. *Protocols for satellite ocean colour data validation: in situ optical radiometry*. In: Zibordi, G., Voss, K.J., Johnson, B.C., Mueller, J.L. (Eds.), *IOCCG Ocean Optics and Biogeochemistry Protocols for Satellite Ocean Colour Sensor Validation*, Volume 3.0. IOCCG, Dartmouth, NS, Canada. <https://doi.org/10.25607/OBP-691>.
- IOCCG Protocol Series, 2021. *Particulate organic matter sampling and measurement protocols: consensus towards future ocean color missions*. In: Chaves, J.E., Cetinić, I., Dall'Olmo, G., Estapa, M., Gardner, W., Goni, M., Graff, J.R., Hernes, P., Lam, P.J., Liu, Z., Lomas, M.W., Mannino, M., Novak, M.G., Turnewitsch, R., Werdell, P.J., Westberry, T.K. (Eds.), *IOCCG Ocean Optics and Biogeochemistry Protocols for Satellite Ocean Colour Sensor Validation*, Volume 6.0. IOCCG, Dartmouth, NS, Canada. <https://doi.org/10.25607/OBP-1646>.
- Johnsen, S., Gassman, E., Reynolds, R.A., Stramski, D., Mobley, C., 2014. The asymmetry of the underwater light field and its implications for mirror-based camouflage in silvery pelagic fish. *Limnol. Oceanogr.* 59, 1839–1852.
- Kermack, K.A., Haldane, J.B.S., 1950. Organic correlation and allometry. *Biometrika* 37, 30–41.
- Koike, I., Hara, S., Terauchi, K., Kogure, K., 1990. Role of sub-micrometre particles in the ocean. *Nature* 345, 242–244.
- Kostadinov, T.S., Milutinović, S., Marinov, I., Cabré, A., 2016. Carbon-based phytoplankton size classes retrieved via ocean color estimates of the particle size distribution. *Ocean Sci.* 12, 561–575. <https://doi.org/10.5194/os-12-561-2016>.
- Le, C., Lehrter, J.C., Hu, C., MacIntyre, H., Beck, M.W., 2017. Satellite observation of particulate organic carbon dynamics on the Louisiana continental shelf. *J. Geophys. Res. Oceans* 122, 555–569.
- Le, C., Zhou, X., Hu, C., Lee, Z., Li, L., Stramski, D., 2018. A color-index-based empirical algorithm for determining particulate organic carbon concentration in the ocean from satellite observations. *J. Geophys. Res. Oceans* 123, 7407–7419.
- Lee, S., Fuhrman, J.A., 1987. Relationships between biovolume and biomass of naturally derived marine bacterioplankton. *Appl. Environ. Microbiol.* 53, 1298–1303.
- Lee, S., Kang, Y.-C., Fuhrman, J.A., 1995. Imperfect retention of natural bacterioplankton cells by glass fiber filters. *Mar. Ecol. Prog. Ser.* 119, 285–290.
- Lee, C., Murray, D.W., Barber, R.T., Buesseler, K.O., Dymond, J., Hedges, J.I., Honjo, S., Manganini, S.J., Marra, J., Moser, C., Peterson, M.L., Prell, W.L., Wakeham, S.G., 1998. Particulate organic carbon fluxes: compilation of results from the 1995 US JGOFS Arabian Sea Process Study. *Deep-Sea Res. II* 45, 2489–2501.
- Legendre, L., Michaud, J., 1999. Chlorophyll *a* to estimate the particulate organic carbon available as food for large zooplankton in the euphotic zone of oceans. *J. Plankton Res.* 21, 2067–2083.
- Li, W.K.W., Dickie, P.M., 1985. Growth of bacteria in seawater filtered through 0.2 μ m Nuclepore membranes: implications for dilution experiments. *Mar. Ecol. Prog. Ser.* 26, 245–252.
- Li, L., Stramski, D., Reynolds, R.A., 2016. Effects of inelastic radiative processes on the determination of water-leaving spectral radiance from extrapolation of underwater near-surface measurements. *Appl. Opt.* 55, 7050–7067.
- Lipsky, J. (Ed.), 2001. *AMLR 2000/2001 Field Season Report Objectives, Accomplishments and Tentative Conclusions*. NOAA-TM-NMFS-SWFC-314. NOAA Southwest Fisheries Science Center, La Jolla, California, 189 pp.
- Liu, D., Pan, D., Bai, Y., He, X., Wang, D., Wei, J.-A., Zhang, L., 2015. Remote sensing observation of particulate organic carbon in the Pearl River Estuary. *Remote Sens.* 7, 8683–8704. <https://doi.org/10.3390/rs70708683>.
- Loisel, H., Bosc, E., Stramski, D., Oubelkheir, K., Deschamps, P.-Y., 2001. Seasonal variability of the backscattering coefficient in the Mediterranean Sea based on satellite SeaWiFS imagery. *Geophys. Res. Lett.* 28, 4203–4206.
- Loisel, H., Nicolas, J.-M., Deschamps, P.-Y., Frouin, R., 2002. Seasonal and inter-annual variability of particulate organic matter in the global ocean. *Geophys. Res. Lett.* 29, 2196. <https://doi.org/10.1029/2002GL015948>.
- Lovечchio, E., Gruber, N., Münnich, M., Lachkar, Z., 2017. On the long-range offshore transport of organic carbon from the Canary Upwelling System to the open North Atlantic. *Biogeosciences* 14, 3337–3369.
- Marra, J., Trees, C.C., Bidigare, R.R., Barber, R.T., 2000. Pigment absorption and quantum yields in the Arabian Sea. *Deep-Sea Res. Part II* 47, 1279–1299.
- Matsuoka, A., Bricaud, A., Benner, R., Para, J., Sempéré, R., Prieur, L., Bélanger, S., Babin, M., 2012. Tracing the transport of colored dissolved organic matter in water masses of the southern Beaufort Sea: relationship with hydrographic characteristics. *Biogeosciences* 9, 925–940.
- Menzel, D.W., 1966. Bubbling of seawater and the production of organic particles: a re-evaluation. *Deep-Sea Res.* 13, 963–966.
- Menzel, D.W., Vaccaro, R.F., 1964. The measurement of dissolved organic and particulate carbon in seawater. *Limnol. Oceanogr.* 9, 138–142.
- Mishonov, A.V., Gardner, W.D., Richardson, M.J., 2003. Remote sensing and surface POC concentration in the South Atlantic. *Deep-Sea Res. II Top. Stud. Oceanogr.* 50, 2997–3015.
- Moran, S.B., Charette, M.A., Pike, S.M., Wicklund, C.A., 1999. Differences in seawater particulate organic carbon concentration in samples collected using small- and large-volume methods: the importance of DOC adsorption to the filter blank. *Mar. Chem.* 67, 33–42.
- Morel, A., 1980. In-water and remote measurements of ocean color. *Bound.-Layer Meteorol.* 18, 177–201.
- Mueller, J.L., 2003. Overview of measurement and data analysis methods. In: Mueller, J.L., Fargion, G.S., McClain, C.R. (Eds.), *Ocean Optics Protocols for Satellite Ocean Color Sensor Validation*, Revision 4, Volume III: Radiometric Measurements and Data Analysis Protocols, NASA Tech. Memo. 2003–211621/Revision 4 Vol. III. NASA Goddard Space Flight Center, Greenbelt, Maryland, pp. 1–20.
- Mueller, J.L., Austin, R.W., 1995. Ocean optics protocols for SeaWiFS validation, Revision 1. In: Hooker, S.B., Firestone, E.R., Acker, J.G. (Eds.), *NASA Tech. Memo. 104566*, Vol. 25. NASA Goddard Space Flight Center, Greenbelt, Maryland, 66 pp.
- Novak, M.G., Cetinić, I., Chaves, J.E., Mannino, A., 2018. The adsorption of dissolved organic carbon onto glass fiber filters and its effect on the measurement of particulate organic carbon: A laboratory and modeling exercise. *Limnol. Oceanogr. Methods* 16, 356–366.
- O'Reilly, J.E., Maritorena, S., O'Brien, M., Siegel, D., Toole, P., Menzies, D., Smith, R., Mueller, J., Mitchell, G., Kahru, M., Chavez, F., Strutton, P., Cota, G., Hooker, S., McClain, C., Carder, K., Muller-Karger, F., Harding, L., Magnuson, A., Phinney, D., Moore, G., Aiken, J., Arriaga, K., Letelier, R., Culver, M., 2000. Ocean color chlorophyll-*a* algorithms for SeaWiFS, OC2and OC4: Version 4. In: Hooker, S.B., Firestone, E.R. (Eds.), *SeaWiFS Postlaunch Calibration and Validation Analyses Part 3*, NASA Tech. Memo. 2000-206892 Vol. 11. NASA Goddard Space Flight Center, Greenbelt, Maryland, 49 pp.
- O'Reilly, J.E., Werdell, P.J., 2019. Chlorophyll algorithms for ocean color sensors – OC4, OC5 & OC6. *Remote Sens. Environ.* 229, 32–47.
- O'Reilly, J.E., Maritorena, S., Mitchell, G., Siegel, D., Carder, K., Garver, S., Kahru, M., McClain, C.R., 1998. Ocean color chlorophyll algorithms for SeaWiFS. *J. Geophys. Res.* 103, 24937–24953.
- Pabi, S., Arriaga, K.R., 2006. Satellite estimation of marine particulate carbon in waters dominated by different phytoplankton taxa. *J. Geophys. Res.* 111, C09003. <https://doi.org/10.1029/2005JC003137>.
- Reynolds, R.A., Stramski, D., 2019. Optical characterization of marine phytoplankton assemblages within surface waters of the western Arctic Ocean. *Limnol. Oceanogr.* 64, 2478–2496.
- Reynolds, R.A., Stramski, D., Mitchell, B.G., 2001. A chlorophyll-dependent semi-analytical reflectance model derived from field measurements of absorption and backscattering coefficients within the Southern Ocean. *J. Geophys. Res.* 106 (C4), 7125–7138.
- Reynolds, R.A., Stramski, D., Neukermans, G., 2016. Optical backscattering of particles in Arctic seawater and relationships to particle mass concentration, size distribution, and bulk composition. *Limnol. Oceanogr.* 61, 1869–1890.
- Ricker, W.E., 1973. Linear regressions in fishery research. *J. Fish. Res. Board Can.* 30, 409–434.
- Röttgers, R., Doerffer, R., 2007. Measurements of optical absorption by chromophoric dissolved organic matter using a point-source integrating-cavity absorption meter. *Limnol. Oceanogr. Methods* 5, 126–135.
- Rouse Jr., J.W., Haas, R.H., Schell, J.A., Deering, D.W., 1973. Monitoring the Vernal Advancement and Retrogradation (Green Wave Effect) of Natural Vegetation, NASA/GSFC Type II Report for Sept. 1972 – March 1973, Greenbelt, Maryland, 112 pp.
- Rouse Jr., J.W., Haas, R.H., Schell, J.A., Deering, D.W., 1974. Monitoring vegetation systems in the Great Plains with ERTS. In: *Proceedings, Third Earth Resources Technology Satellite-1 Symposium*, NASA SP-351, Greenbelt, Maryland, pp. 309–317.
- Seegers, B.N., Stumpf, R.P., Schaeffer, B.A., Loftin, K.A., Werdell, P.J., 2018. Performance metrics for the assessment of satellite data products: an ocean color case study. *Opt. Express* 26, 7404–7442.
- Sharp, J.H., 1973. Size classes of organic carbon in seawater. *Limnol. Oceanogr.* 18, 441–447.
- Sheldon, R.W., 1972. Size separation of marine seston by membrane and glass fiber filters. *Limnol. Oceanogr.* 17, 494–498.
- Shiozaki, T., Ijichi, M., Fujiwara, A., Makabe, A., Nishino, S., Yoshikawa, C., Harada, N., 2019. Factors regulating nitrification in the Arctic Ocean: Potential impact of sea ice reduction and ocean acidification. *Glob. Biogeochem. Cycles* 33, 1085–1099. <https://doi.org/10.1029/2018GB006068>.

- Smith Jr., W.O., Anderson, R.F., Moore, J.K., Codispoti, L.A., Morrison, J.M., 2000. The US Southern Ocean Joint Global Ocean Flux Study: an introduction to AESOPS. *Deep-Sea Res. II* 47, 3073–3093.
- Smith, S.L., Codispoti, L.A., Morrison, J.M., 1998. The 1994–1996 Arabian Sea Expedition: An integrated, interdisciplinary investigation of the response of the northwestern Indian Ocean to monsoonal forcing. *Deep-Sea Res. II* 45, 1905–1915.
- Sokal, R.R., Rohlf, F.J., 1995. *Biometry: The Principles and Practice of Statistics in Biological Research*, 3rd edition., W. H. Freeman and Co., New York., 880 pp.
- Son, Y.B., Gardner, W.D., Mishonov, A.V., Richardson, M.J., 2009. Multispectral remote-sensing algorithms for particulate organic carbon (POC): The Gulf of Mexico. *Remote Sens. Environ.* 113, 50–61.
- Stow, C.A., Jolliff, J., McGillicuddy, D.J., Doney, S.C., Allen, J.I., Friedrichs, M.A.M., Rose, K.A., Wallhead, P., 2009. Skill assessment for coupled biological/physical models of marine systems. *J. Mar. Syst.* 76, 4–15.
- Stramska, M., 2009. Particulate organic carbon in the global ocean derived SeaWiFS ocean color. *Deep-Sea Res. I* 56, 1459–1470.
- Stramska, M., Cieszyńska, A., 2015. Ocean colour estimates of particulate organic carbon reservoirs in the global ocean – revisited. *Int. J. Remote Sens.* 35, 3675–3700.
- Stramski, M., Stramski, D., 2005. Variability of particulate organic carbon concentration in the north polar Atlantic based on ocean color observations with Sea-viewing Wide Field-of-view Sensor (SeaWiFS). *J. Geophys. Res.* 110, C10018. <https://doi.org/10.1029/2004jc002762>.
- Stramski, D., 1990. Artifacts in measuring absorption spectra of phytoplankton collected on a filter. *Limnol. Oceanogr.* 35, 1804–1809.
- Stramski, D., Kiefer, D.A., 1991. Light scattering by microorganisms in the open ocean. *Prog. Oceanogr.* 28, 343–383.
- Stramski, D., Woźniak, S.B., 2005. On the role of colloidal particles in light scattering in the ocean. *Limnol. Oceanogr.* 50, 1581–1591.
- Stramski, D., Reynolds, R.A., Kahru, M., Mitchell, B.G., 1999. Estimation of particulate organic carbon in the ocean from satellite remote sensing. *Science* 285, 239–242.
- Stramski, D., Darecki, M., Stramska, M., 2006. Bio-optical relationships for estimating particulate organic carbon concentration in the upper ocean derived from historical data. *EOS Trans. AGU* 87 (36). *Ocean Sci. Meet. Suppl.*, Abstract OS25G-10.
- Stramski, D., Reynolds, R.A., Babin, M., Kaczmarek, S., Lewis, M.R., Röttgers, R., Sciadra, A., Stramska, M., Twardowski, M.S., Franz, B.A., Claustre, H., 2008. Relationships between the surface concentration of particulate organic carbon and optical properties in the eastern South Pacific and eastern Atlantic Oceans. *Biogeosciences* 5, 171–201.
- Taguchi, S., Laws, E.A., 1988. On the microparticles which pass through glass fiber filter type GF/F in coastal and open waters. *J. Plankton Res.* 10, 999–1008.
- Tran, T.K., Duforêt-Gaurier, L., Vantrepotte, V., Jorge, D.S.F., Mériaux, X., Cauvin, A., Fanton d'Andon, O., Loisel, H., 2019. Deriving particulate organic carbon in coastal waters from remote sensing: Inter-comparison exercise and development of a maximum band-ratio approach. *Remote Sens.* 11, 2849. <https://doi.org/10.3390/rs11232849>.
- Turnewitsch, R., Springer, B.M., Kiriakoulakis, K., Vilas, J.C., Aristegui, J., Wolff, G., Peine, F., Werk, S., Graf, G., Waniek, J.J., 2007. Determination of particulate organic carbon (POC) in seawater: The relative methodological importance of artificial gains and losses in two glass-fiber-filter-based techniques. *Mar. Chem.* 105, 208–228.
- Uitz, J., Stramski, D., Reynolds, R.A., Dubranna, J., 2015. Assessing phytoplankton community composition from hyperspectral measurements of phytoplankton absorption coefficient and remote-sensing reflectance in open-ocean environments. *Remote Sens. Environ.* 171, 58–74.
- Valente, A., Sathyendranath, S., Brotas, V., Groom, S., Grant, M., Taberner, M., Antoine, D., Arnone, R., Balch, W.M., Barker, K., Barlow, R., Bélanger, S., Berthon, J.-F., Besiktepe, S., Brando, V., Canuti, E., Chavez, F., Claustre, H., Crout, R., Frouin, R., García-Soto, C., Gibb, S.W., Gould, R., Hooker, S., Kahru, M., Klein, H., Kratzer, S., Loisel, H., McKee, D., Mitchell, B.G., Moisan, T., Muller-Karger, F., O'Dowd, L., Ondrusek, M., Poulton, A.J., Repecaud, M., Smyth, T., Sosik, H.M., Twardowski, M., Voss, K., Werdell, J., Wernand, M., Zibordi, G., 2016. A compilation of global bio-optical in situ data for ocean-colour satellite applications. *Earth Syst. Sci. Data* 8, 235–252. <https://doi.org/10.5194/essd-8-235-2016>.
- Valente, A., Sathyendranath, S., Brotas, V., Groom, S., Grant, M., Taberner, M., Antoine, D., Arnone, R., Balch, W.M., Barker, K., Barlow, R., Bélanger, S., Berthon, J.-F., Besiktepe, S., Borsheim, Y., Bracher, A., Brando, V., Canuti, E., Chavez, F., Cianca, A., Claustre, H., Clementson, L., Crout, R., Frouin, R., García-Soto, C., Gibb, S.W., Gould, R., Hooker, S., Kahru, M., Kampel, M., Klein, H., Kratzer, S., Kudela, R., Ledesma, J., Loisel, H., Matrai, P., McKee, D., Mitchell, B.G., Moisan, T., Muller-Karger, F., O'Dowd, L., Ondrusek, M., Platt, T., Poulton, A.J., Repecaud, M., Schroeder, T., Smyth, T., Smythe-Wright, D., Sosik, H.M., Twardowski, M., Vellucci, V., Voss, K., Werdell, J., Wernand, M., Wright, S., Zibordi, G., 2019. A compilation of global bio-optical in situ data for ocean-colour satellite applications – version two. *Earth Syst. Sci. Data* 11, 1037–1068. <https://doi.org/10.5194/essd-11-1037-2019>.
- Vandermeulen, R.A., Mannino, A., Craig, S.E., Werdell, P.J., 2020. 150 shades of green: Using the full spectrum of remote sensing reflectance to elucidate color shifts in the ocean. *Remote Sens. Environ.* 247, 111900.
- Volk, T., Hoffert, M.I., 1985. Ocean carbon pumps: Analysis of relative strengths and efficiencies in ocean-driven atmospheric CO₂ changes. In: Sundquist, E.T., Broecker, W.S. (Eds.), *The Carbon Cycle and Atmospheric CO₂: Natural Variations Archean to Present*, Geophys. Monogr. Ser., vol. 32. AGU, Washington, D. C., pp. 99–110.
- Volkman, J.K., Tanoue, E., 2002. Chemical and biological studies of particulate organic matter in the ocean. *J. Oceanogr.* 58, 265–279.
- Wakeham, S.G., Lee, C., 1993. Production, transport, and alteration of particulate organic matter in the marine water column. In: Engel, M.H., Macko, S.A. (Eds.), *Organic Geochemistry*. Plenum Press, pp. 145–169.
- Wells, M.L., Goldberg, E.D., 1992. Marine submicron particles. *Mar. Chem.* 40, 5–18.
- Wells, M.L., Goldberg, E.D., 1994. The distribution of colloids in the North Atlantic and Southern Oceans. *Limnol. Oceanogr.* 39, 286–302.
- Woźniak, S.B., Stramski, D., Stramska, M., Reynolds, R.A., Wright, V.M., Miksic, E.Y., Cichocka, M., Cieplak, A.M., 2010. Optical variability of seawater in relation to particle concentration, composition, and size distribution in the nearshore marine environment at Imperial Beach, California. *J. Geophys. Res.* 115, C08027. <https://doi.org/10.1029/2009jc005554>.
- Woźniak, S.B., Darecki, M., Zabłocka, M., Burska, D., Dera, J., 2016. New simple statistical formulas for estimating surface concentrations of suspended particulate matter (SPM) and particulate organic carbon (POC) from remote-sensing reflectance in the southern Baltic Sea. *Oceanologia* 58, 161–175.
- Zhang, X., Hu, L., Xiong, Y., Huot, Y., Gray, D., 2020. Experimental estimates of optical backscattering associated with submicron particles in clear oceanic waters. *Geophys. Res. Lett.* 47 e2020GL087100.
- Zheng, G., Stramski, D., Reynolds, R.A., 2014. Evaluation of the Quasi-Analytical Algorithm for estimating the inherent optical properties of seawater from ocean color: Comparison of Arctic and lower-latitude waters. *Remote Sens. Environ.* 155, 194–209.

SUPPLEMENTARY MATERIAL

for the article entitled "Ocean color algorithms to estimate the concentration of particulate organic carbon in surface waters of the global ocean in support of a long-term data record from multiple satellite missions" by Dariusz Stramski, Ishan Joshi, and Rick A. Reynolds

Measurements of $R_{rs}(\lambda)$

This section of Supplementary Material is pertinent to Section 3.1 in the associated article. On the two cruises in the Pacific, one cruise in the Atlantic (ANTXXVI/4), and one cruise in the Arctic (MR17-05C), the underwater upwelling radiance measurements, $L_u(\lambda, z=0.2 \text{ m})$, were made at a depth z of 0.2 m below the surface with a hyperspectral radiometer mounted on a surface float and operated at significant distance from the vessel (Table 2 in the associated article). These radiance measurements were extrapolated to just below the surface (i.e., $z=0^-$) and then propagated across the water-air interface to determine $L_w(\lambda)$. In parallel to near-surface radiance measurements, the irradiance $E_s(\lambda)$ was measured directly with a spectrally-matched sensor mounted on the ship's mast. Time-series data of $L_w(\lambda)$ and $E_s(\lambda)$ were acquired typically over a few minutes. These data were checked for quality and interpolated to a common time frame and spectral interval before the calculation of final average values of $R_{rs}(\lambda)$ (Stramski et al., 2008).

On the remaining cruises depth profiles of spectrally-matched $L_u(\lambda, z)$ and $E_d(\lambda, z)$ were measured within the ocean surface layer (Table 2 in the associated article). These measurements were made either with free-fall profiling radiometers (SPMR, C-OPS, or PRR-800) deployed at significant distance from the vessel or with a MER-2040 radiometer deployed from the side of the ship facing the direction of the sun. The methodology of processing the depth profile data involved several common steps which include: (i) data quality control (e.g., rejection of very different replicate casts or profiles, especially when acquired during variable sky conditions) and binning the data into depth intervals ranging from 0.1 to 1 m depending on the cruise (ii) determination of surface layer delimited by the depths of z_1 and z_2 (where z_1 typically ranges between about 1 and 5 m and z_2 between 3 m and 20 m depending on environmental conditions under which the measurements were made) such that the vertical attenuation of $L_u(\lambda)$ and $E_d(\lambda)$ for any given light wavelength within the z_1 - z_2 layer is well approximated by single values of the diffuse attenuation coefficients of $L_u(\lambda)$ and $E_d(\lambda)$, (iii) extrapolation of $L_u(\lambda)$ and $E_d(\lambda)$ from z_1 to just below the surface (i.e., $z=0^-$) using the values of the diffuse attenuation coefficients, and (iv) propagation of $L_u(\lambda, z=0^-)$ and $E_d(\lambda, z=0^-)$ across the water-air interface to determine the desired values of $L_w(\lambda)$ and $E_s(\lambda)$. Between the cruises there were small inconsequential differences in the values of water-to-air transmittance coefficients that were used to multiply $L_u(\lambda, z=0^-)$ and $E_d(\lambda, z=0^-)$ to obtain $L_w(\lambda)$ and $E_s(\lambda)$. For radiance these coefficients varied between 0.54 and 0.543 and for irradiance between 1/0.957 and 1/0.97 (e.g., Antoine et al., 2013; Stramski et al., 2008).

As described in the associated article (Section 3.1), the $R_{rs}(\lambda)$ measurements obtained with multispectral radiometers were interpolated using Piecewise Cubic Hermite Interpolating Polynomial (PCHIP) to produce $R_{rs}(\lambda)$ values at all wavelengths required for development of POC algorithms for different ocean color sensors. Before selecting the PCHIP method we compared its performance with two other interpolation methods, a linear interpolation of $R_{rs}(\lambda)$ data and a linear interpolation of log-transformed $R_{rs}(\lambda)$ data (e.g., O'Reilly and Werdell, 2019). In this analysis we

used the final hyperspectral data (1-nm interval) from the BIOSOPE, KM12-10, ANTXXVI/4, and MR17-05C cruises. These hyperspectral data were first spectrally subsampled at appropriate wavelengths to create multispectral datasets simulating measurements with the multispectral radiometers, i.e., SPMR, two MER-2040 instruments, C-OPS, and PRR-800 (see Table 2 in the paper). Then, these multispectral data were subject to the three interpolation methods and the interpolation results were compared with the measured hyperspectral data. Although the differences in the performance of the three interpolation methods were small, the PCHIP interpolated data were most consistent in terms of exhibiting a very good to excellent agreement with measured data (to within a few percent) within the blue-green spectral region for all multispectral scenarios.

Comparative analysis of various candidate algorithms

This section of Supplementary Material is pertinent to Section 4 in the associated article. Here we provide a summary of the results describing the comparative analysis of all candidate algorithm categories. This analysis is demonstrated for SeaWiFS bands but similar analysis was also made for other ocean color sensors. Table S1 provides the best-fit regression formula for each of the seven algorithm categories (i.e., CAT1 through CAT7 as described in Section 4 of the associated article) investigated in this study. These formulas were obtained from robust regression analysis applied to our algorithm development dataset consisting of 139 pairs of POC and $R_{rs}(\lambda)$ measurements. For a given algorithm category, the formula presented in Table S1 provided better fit to the data than other candidate formulas which were examined for that category. For the CAT1 (BR-PF) category the best-fit formula uses a single blue-to-green band ratio. For the CAT2 (MBR) category the best formula is based on a maximum value selected from three band ratios which involve four light wavelengths. This formula is referred to as MBR-OC4. For the CAT3 category, Table S1 includes two formulations; one is based solely on CI and the other is based on the combination of CI and MBR components operating in different ranges of POC. The CAT3 (CI) is analogous to the approach of Le et al. (2018) and involves the use of three light wavelengths. The CAT3 (CI+MBR) is analogous to the approach used in chlorophyll algorithm (Hu et al., 2012) and involves five wavelengths. Note that the MBR-OC4 formulas in CAT2 (MBR) and CAT3 (CI+MBR) are the same. For the CAT4 (NDCI) category the best formula uses a maximum value selected from two individual NDCI variables. This formula involves three wavelengths. For CAT5 (mNDCI) category the algorithm formula is based on the use of four wavelengths. For CAT6 (BRDI) category the best formula uses a maximum value selected from two individual BRDI variables which altogether involve four wavelengths. Importantly, we note that this formula is referred to as MBRDI in the associated article. In Supplementary Material related to Tables S1, S2 and S3 as well as Fig S1 we refer to this algorithm using a general symbol BRDI of CAT6 category while recognizing that the best formula for the entire development dataset from this category is based on $BRDI \equiv MBRDI$ as defined in Table S1. Finally, for the CAT7 (MLR) category the best formula was identified as a 2-band version of multiple linear regression.

Figure S1 illustrates how the best regression formula from each category (except for CAT7 Multiple Regression Analysis which is not shown) fits the algorithm development dataset. Note that for the CAT3 (CI+MBR) algorithm (Fig. S1d), the fitted curve is shown only for the CI

component of the algorithm which operates within the range of relatively low POC. The vertical dashed lines in Fig. S1 represent the values of explanatory variable involving $R_{rs}(\lambda)$ which correspond to hypothetical ocean consisting of pure seawater only. These values were obtained from radiative transfer simulations assuming a solar zenith angle of 30° and a wind speed of 5 m s^{-1} (Li et al., 2016). It is instructive to compare the POC values predicted by each algorithm when its explanatory variable assumes the value corresponding to pure seawater condition. These POC values are: 11.7 mg m^{-3} for CAT1 (BR-PF), 10 mg m^{-3} for CAT2 (MBR), 23.2 mg m^{-3} for CAT3 (CI), 14 mg m^{-3} for CAT3 (CI+MBR), 11.9 mg m^{-3} for CAT4 (NDCI), 11.7 mg m^{-3} for CAT5 (mNDCI), and 1.5 mg m^{-3} for CAT6 (BRDI). This comparison shows that all algorithms except CAT6 (BRDI) predict POC of about 10 mg m^{-3} or higher for pure seawater condition. The CAT6 (BRDI) algorithm makes a prediction that is significantly closer to $\text{POC} = 0$, which results from greater curvature of this algorithm at very low POC compared to other algorithms. The lowest POC in our dataset is about 12 mg m^{-3} and was measured in ultraoligotrophic waters within the South Pacific subtropical gyre. These waters are among the clearest oceanic waters (Morel et al., 2007), so the POC values of about 10 mg m^{-3} are probably close to the minimum POC that can be encountered in surface ocean waters. While our algorithms are not intended for application outside the range of our development dataset, the curvature of BRDI algorithm at very low POC is advantageous compared with other algorithms. This is because it allows estimation of POC down to the lowest values of POC found in surface waters of ultraoligotrophic ocean ($\sim 10 \text{ mg m}^{-3}$ or even below 10 mg m^{-3}) while the BRDI value does not yet reach the pure seawater condition.

Table S2 provides several statistical parameters (see Table 3 in the associated article) which characterize the goodness-of-fit of each algorithm formula from Table S1 for our algorithm development dataset. The selected results of pair-wise comparison between the algorithms are also included. We recall that the algorithm formulas in Table S1 were obtained from the robust regression method but, for comparison purposes, similar results were also obtained with the ordinary least squares (OLS) regression method (not shown). For all algorithms except CAT7 (MLR) the differences between the robust regression and OLS-based statistical parameters were generally very small or indiscernible. This is indicative that our dataset does not include strong “outliers”.

The comparison of statistics in Table S2 across different algorithms indicates that CAT3 (CI) and CAT7 (MLR) are clearly inferior compared to other algorithms. The CAT1 (BR-PF) is also inferior with significantly higher *RMSD*. For the remaining five algorithms the statistical parameters are typically similar. A closer inspection of all statistical results in Table S2 suggests that CAT2 (MBR) with its overall comparatively good statistics and the best pair-wise comparison results against other algorithms is a suitable candidate for consideration in formulation of final algorithms. Table S2 also shows that CAT6 (BRDI), which was demonstrated to have the largest curvature at very low POC (Fig. S1), has comparable statistical parameters to other potential candidate algorithms for the whole range of POC within our dataset.

Table S3 compares the statistical parameters of five best candidate algorithms (as identified in Table S2) for two ranges of POC, $> 25 \text{ mg m}^{-3}$ and $< 20 \text{ mg m}^{-3}$. Note that this comparison is for the algorithm formulas (shown in Table S1) which were fit to the entire dataset, and not tuned specifically to these POC ranges. Because CAT1 (BR-PF), CAT3 (CI) and CAT7 (MLR) showed clearly inferior performance (Table S2), these algorithms are not included in Table S3.

There are two main results coming from Table S3. First, CAT2 (MBR) has generally the best statistical parameters over the range of $\text{POC} > 25 \text{ mg m}^{-3}$. This is the case even though the differences compared with other candidate algorithms are mostly small. This range of POC covers most situations in the ocean with the exception of ultraoligotrophic waters, and includes 121 out of the total of 139 data points in our dataset. We also made similar comparisons for other POC ranges, such as $50 - 100 \text{ mg m}^{-3}$ and $100 - 250 \text{ mg m}^{-3}$ which include reasonably large number of data points in our dataset (45 and 28, respectively) as well as the range of $\text{POC} > 250 \text{ mg m}^{-3}$ with a smaller number of data (10). For these ranges, the suite of the goodness-of-fit statistical parameters indicated that CAT2 (MBR) also provided better fit to the data than other candidate algorithms. These results support the notion that CAT2 (MBR) is a good choice for formulation of final algorithms and that the MBR-OC4 formula is suitable for predicting POC over a very broad range of POC.

The second key result from Table S3 addresses the range of very low $\text{POC} < 20 \text{ mg m}^{-3}$. The CAT2 (MBR) algorithm tends to overestimate very low POC in our dataset, so it is desirable to identify another candidate algorithm for very low POC. Table S3 shows that in this range the CAT6 (BRDI) algorithm has overall the best statistical parameters and pair-wise comparison results although admittedly the number of data available in this range is small ($N = 9$). In addition, as discussed above, the CAT6 (BRDI) algorithm provides an advantage at very low POC owing to its greater curvature compared with other candidate algorithms. It is also noteworthy that compared to other potential candidates for use at very low POC, especially CAT4 (NDCI) and CAT5 (mNDCI) (see also the behavior of these algorithms at very low POC in Fig. S1), the values of BRDI exhibit a larger dynamic range than the values of NDCI or mNDCI within the range of lowest POC found in ultraoligotrophic waters. For example, as POC decreases from 20 to 10 mg m^{-3} , the value of BRDI changes by about 15%, the NDCI by 8%, and the mNDCI by 9%. This result suggests that the CAT6 (BRDI) formulation has better resolving power at these very low levels of POC. The results in Table S3 along with the greater curvature and dynamic range of CAT6 (BRDI) function at very low POC support the notion that this algorithm is a good choice for consideration in formulation of final algorithms to provide predictions of POC in the range of very low levels found in ultraoligotrophic waters. Thus, CAT2 (MBR) and CAT6 (BRDI) were selected for further analysis and formulation of final hybrid algorithms as described in Section 5 of the associated article.

Table S1. The best-fit regression functions for different algorithm categories which were determined by application of robust regression method to our algorithm development dataset ($N = 139$). All regression functions were fitted to all data from the development dataset except for the CI algorithms. The CAT3 (CI) algorithm consist of two functions which were fitted to subsets of our development dataset within the two ranges of CI as indicated in the table ($N = 106$ for $CI < -0.0005$ and $N = 33$ for $CI \geq -0.0005$). The CI component of the CAT3 (CI+MBR) algorithm was fitted to subset of data with $POC < 70 \text{ mg m}^{-3}$ ($N = 89$).

Category	Algorithm	Formula of regression function	a_0	a_1	a_2	a_3	a_4	a_5
CAT1	BR-PF	$\log(POC) = a_0 + a_1 \log(X)$ where $X = \frac{R_{rs}(443)}{R_{rs}(555)}$	2.3314	-1.0549	—	—	—	—
CAT2	MBR	$\log(POC) = a_0 + a_1 [\log(X)] + a_2 [\log(X)]^2 + a_3 [\log(X)]^3$ where $X \equiv MBR = \max \left[\frac{R_{rs}(443)}{R_{rs}(555)}, \frac{R_{rs}(490)}{R_{rs}(555)}, \frac{R_{rs}(510)}{R_{rs}(555)} \right]$	2.5037	-2.1297	1.8727	-0.9554	—	—
CAT3	CI	$\log(POC) = a_0 + a_1 X$ for $CI < -0.0005$ $\log(POC) = a_0 + a_1 X$ for $CI \geq -0.0005$ where $X \equiv CI = R_{rs}(555) - \left[R_{rs}(490) + \left(\frac{555-490}{670-490} \right) (R_{rs}(670) - R_{rs}(490)) \right]$	2.0516 2.2007	208.5610 274.9562	— —	— —	— —	— —
	CI+MBR	For $POC_{MBR} < 50 \text{ mg m}^{-3}$ $\log(POC_{CI}) = a_0 + a_1 X$ where $X \equiv CI = R_{rs}(555) - \left[R_{rs}(443) + \left(\frac{555-443}{670-443} \right) (R_{rs}(670) - R_{rs}(443)) \right]$ For $POC_{MBR} > 70 \text{ mg m}^{-3}$ $\log(POC_{MBR}) = a_0 + a_1 [\log(X)] + a_2 [\log(X)]^2 + a_3 [\log(X)]^3$ where $X \equiv MBR = \max \left[\frac{R_{rs}(443)}{R_{rs}(555)}, \frac{R_{rs}(490)}{R_{rs}(555)}, \frac{R_{rs}(510)}{R_{rs}(555)} \right]$ The CI and MBR algorithms are merged in the range $50 \leq POC_{MBR} \leq 70 \text{ mg m}^{-3}$ using a weighting approach*	1.8732 2.5037	90.0432 -2.1297	— 1.8727	— -0.9554	— —	— —
CAT4	NDCI	$\log(POC) = a_0 + a_1 X + a_2 X^2 + a_3 X^3 + a_4 X^4 + a_5 X^5$ where $X \equiv NDCI = \max \left[\frac{R_{rs}(490) - R_{rs}(555)}{R_{rs}(490) + R_{rs}(555)}, \frac{R_{rs}(510) - R_{rs}(555)}{R_{rs}(510) + R_{rs}(555)} \right]$	2.5281	-1.7279	-0.0503	-2.2132	14.0994	-16.1412
CAT5	mNDCI	$\log(POC) = a_0 + a_1 X + a_2 X^2 + a_3 X^3 + a_4 X^4 + a_5 X^5$ where $X \equiv mNDCI = \frac{R_{rs}(555) - \max[R_{rs}(443), R_{rs}(490), R_{rs}(510)]}{R_{rs}(555) + \max[R_{rs}(443), R_{rs}(490), R_{rs}(510)]}$	2.5169	1.7134	0.7229	2.4062	7.2708	6.1462
CAT6	BRDI	$\log(POC) = a_0 + a_1 X + a_2 X^2 + a_3 X^3 + a_4 X^4 + a_5 X^5$ where $X \equiv BRDI = \max \left[\frac{R_{rs}(443) - R_{rs}(555)}{R_{rs}(490)}, \frac{R_{rs}(490) - R_{rs}(555)}{R_{rs}(510)} \right]$	2.5037	-0.8498	-0.1692	-0.2269	0.0504	-0.0536
CAT7	MLR	$\log(POC) = a_0 + a_1 R_{rs}(490) + a_2 R_{rs}(555)$	1.8486	-140.5413	361.5335	—	—	—

* Weighting approach:

$POC = POC_{MBR} W_{MBR} + POC_{CI} W_{CI}$ where $W_{MBR} = 0.5[w_{MBR} + (1 - w_{CI})]$ and $W_{CI} = 1 - W_{MBR}$

Calculation of weighting factors w_{MBR} and w_{CI}

$w_{MBR} = 1$ for $POC_{MBR} > 70 \text{ mg m}^{-3}$

$w_{MBR} = (POC_{MBR} - 50)/(70 - 50)$ for $50 \leq POC_{MBR} \leq 70 \text{ mg m}^{-3}$

$w_{MBR} = 0$ for $POC_{MBR} < 50 \text{ mg m}^{-3}$

$w_{CI} = 0$ for $POC_{CI} > 70 \text{ mg m}^{-3}$

$w_{CI} = (POC_{CI} - 70)/(50 - 70)$ for $50 \leq POC_{CI} \leq 70 \text{ mg m}^{-3}$

$w_{CI} = 1$ for $POC_{CI} < 50 \text{ mg m}^{-3}$

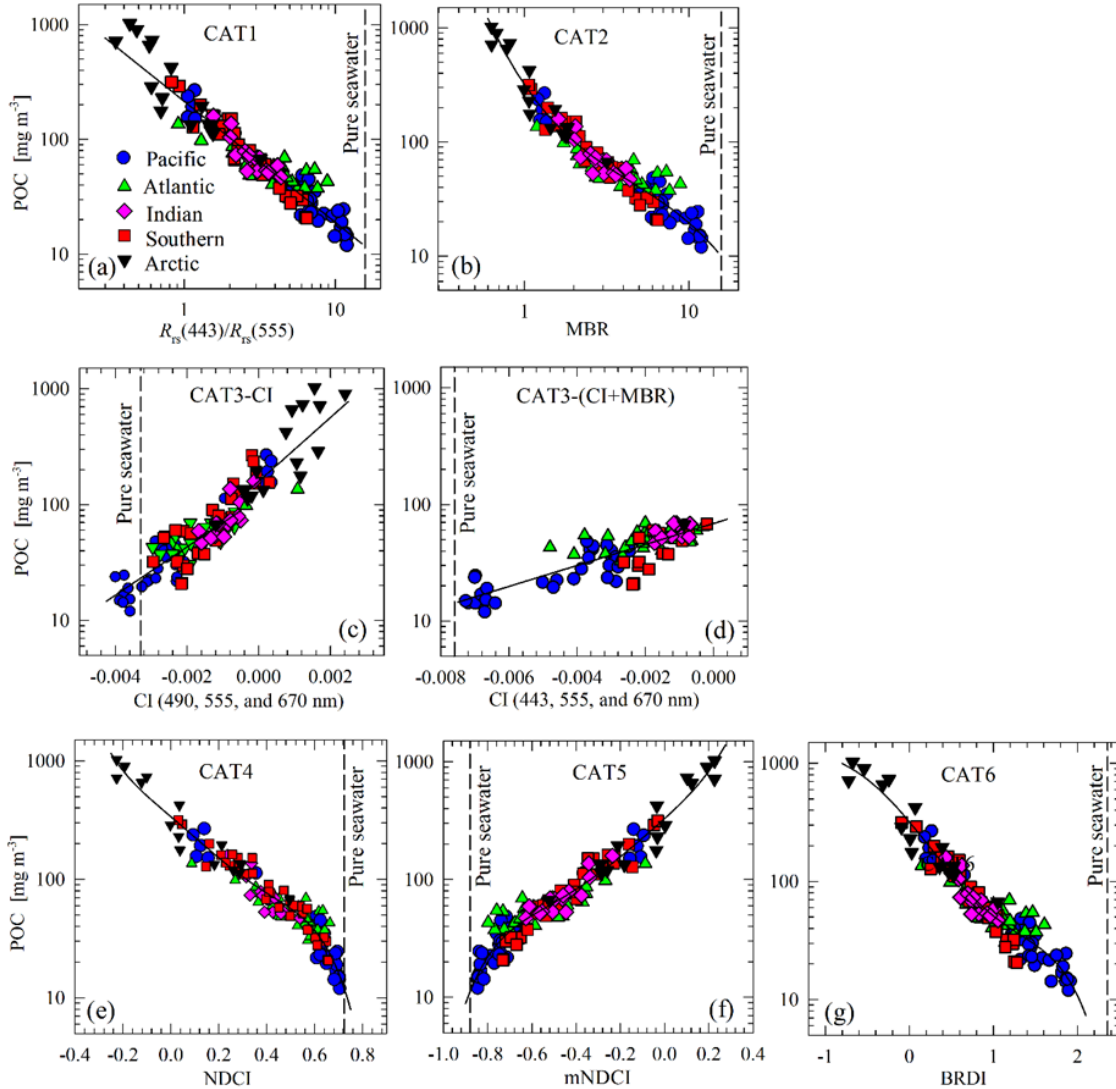


Fig. S1. The best-fit regression functions for different algorithm categories (solid lines, the formulas shown in Table S1) and all data comprising our algorithm development dataset. Data from different ocean basins are depicted using different symbols as indicated in panel (a). In panel (d) only the CI component of the CAT3 (CI+MBR) algorithm is shown for the range of $POC < 70 \text{ mg m}^{-3}$. In each panel an approximate value of explanatory variable (horizontal axis) for the case of pure seawater is also shown as dotted line.

Table S2. The goodness-of-fit statistical parameters and selected results of pair-wise comparisons for best-fit regression functions from different algorithm categories shown in Table S1. The statistical parameters are explained in Table 3 in the associated article.

Statistical parameter	CAT1	CAT2	CAT3		CAT4	CAT5	CAT6	CAT7
	BR-PF	MBR	CI	CI+MBR	NDCI	mNDCI	BRDI	MLR
<i>R</i>	0.95	0.97	0.93	0.96	0.97	0.97	0.96	0.89
<i>S</i>	0.95	0.98	0.93	0.96	0.98	0.98	0.97	1.08
<i>A</i>	1.23	1.09	1.32	1.20	1.10	1.10	1.15	0.74
<i>MdR</i>	0.99	0.99	1.01	1.00	0.99	1.00	0.99	1.03
<i>MdB</i> (mg m ⁻³)	-0.24	-0.19	0.59	-0.14	-0.39	-0.10	-0.58	0.85
<i>MdAPD</i> (%)	16.11	13.85	20.55	15.65	14.66	14.84	14.68	19.74
<i>RMSD</i> (mg m ⁻³)	75.45	41.71	91.07	42.84	40.52	40.76	42.64	273.89
<i>MdAE_{log}</i>	1.19	1.15	1.23	1.18	1.17	1.16	1.16	1.20
% wins of MBR	64	—	85	58	51	51	51	60
% wins of BRDI	56	48	86	53	49	50	—	61

Table S3. The selected goodness-of-fit statistical parameters and results of pair-wise comparisons for best-fit regression functions from five algorithm categories (shown in Table S1) for two ranges of POC, > 25 mg m⁻³ and < 20 mg m⁻³.

Statistical parameter	CAT2	CAT3	CAT4	CAT5	CAT6
	MBR	CI+MBR	NDCI	mNDCI	BRDI
POC > 25 mg m ⁻³ (N = 121)					
<i>MdR</i>	0.98	0.98	0.98	0.97	0.98
<i>MdB</i> (mg m ⁻³)	-1.20	-1.29	-2.28	-1.98	-1.77
<i>MdAPD</i> (%)	13.37	15.33	14.50	13.42	14.64
<i>RMSD</i> (mg m ⁻³)	41.65	41.70	42.47	41.70	42.54
<i>MdAE_{log}</i>	1.15	1.17	1.16	1.15	1.17
% wins of MBR	—	52	53	49	51
POC < 20 mg m ⁻³ (N = 9)					
<i>MdR</i>	1.08	1.13	1.10	1.08	1.06
<i>MdB</i> (mg m ⁻³)	1.19	1.86	1.43	1.20	0.99
<i>MdAPD</i> (%)	9.19	13.02	9.67	9.74	7.55
<i>RMSD</i> (mg m ⁻³)	0.86	0.84	0.85	0.84	0.94
<i>MdAE_{log}</i>	1.10	1.13	1.10	1.11	1.09
% wins of BRDI	67	57	67	67	—

Statistical parameters of final hybrid algorithms

Table S4 is pertinent to Section 6 in the associated article and provides the goodness-of-fit statistical parameters for all final hybrid algorithm formulations which are shown in Table 4 in the associated article. These results represent the entire algorithm development dataset with original POC measurements ($N = 139$).

Table S5 is pertinent to Section 8 in the associated article and provides the goodness-of-fit statistical parameters for all final hybrid algorithm formulations which are shown in Table 5 in the associated article. These results represent the dataset with POC measurements corrected for DOC adsorption ($N = 107$).

As explained in the associated article, it is important to recall here that the BRDI component of the final hybrid algorithms is not the same as the best formula selected from CAT6 (BRDI) which is presented in Table S1. While the CAT6 (BRDI) formula in Table S1 represents the best fit to the entire algorithm development dataset using the maximum value of two individual BRDI variables, the BRDI algorithm involved as a component of the final hybrid algorithm aims at estimation of very low POC values and was obtained by fitting one individual BRDI variable to data with $\text{POC} < 70 \text{ mg m}^{-3}$. This BRDI variable in the final hybrid algorithms involves three wavelengths, for example 443, 490 and 555 nm for SeaWiFS sensor.

Table S4. The goodness-of-fit statistical parameters for final hybrid algorithms for different ocean color sensors which are based on the algorithm development dataset ($N = 139$). These final algorithms are described in Table 4 in the associated article. The statistical parameters are explained in Table 3 in the associated article.

Sensor	Hybrid algorithm	R	S	A	MdR	MdB (mg m^{-3})	$MdAPD$ (%)	$RMSD$ (mg m^{-3})	$MdAE_{log}$
SeaWiFS	BRDI+MBR-OC4	0.97	0.98	1.08	0.99	-0.32	13.65	41.71	1.15
MODIS	BRDI+MBR-OC3	0.96	0.97	1.12	1.00	0.43	15.05	51.57	1.17
	BRDI+MBR-OC4	0.96	0.97	1.11	1.01	0.30	14.55	44.94	1.16
VIIRS-SNPP	BRDI+MBR-OC3	0.96	0.97	1.11	0.99	-0.34	15.53	52.94	1.18
	BRDI+MBR-OC4	0.96	0.98	1.10	0.99	-0.13	14.31	45.86	1.16
VIIRS-JPSS-1	BRDI+MBR-OC3	0.96	0.98	1.09	1.00	-0.33	14.75	54.54	1.17
	BRDI+MBR-OC4	0.97	0.98	1.10	0.99	-0.27	13.96	45.42	1.16
MERIS/OLCI	BRDI+MBR-OC4	0.97	0.98	1.07	1.00	0.04	13.99	43.22	1.15

Table S5. The goodness-of-fit statistical parameters for final hybrid algorithms for different ocean color sensors which are based on the algorithm development dataset with POC measurements corrected for DOC adsorption ($N = 107$). These final algorithms are described in Table 5 in the associated article.

Sensor	Hybrid algorithm	R	S	A	MdR	MdB (mg m^{-3})	$MdAPD$ (%)	$RMSD$ (mg m^{-3})	$MdAE_{log}$
SeaWiFS	BRDI+MBR-OC4	0.96	0.98	1.08	1.01	0.25	17.02	48.98	1.19
MODIS	BRDI+MBR-OC3	0.96	0.97	1.13	1.02	0.24	18.22	60.01	1.21
	BRDI+MBR-OC4	0.96	0.97	1.09	1.02	0.41	18.56	51.53	1.21
VIIRS-SNPP	BRDI+MBR-OC3	0.96	0.97	1.11	1.01	0.26	18.26	62.03	1.22
	BRDI+MBR-OC4	0.96	0.97	1.11	1.01	0.35	19.01	51.54	1.20
VIIRS-JPSS-1	BRDI+MBR-OC3	0.96	0.98	1.08	1.01	0.13	18.74	63.61	1.20
	BRDI+MBR-OC4	0.96	0.98	1.09	1.01	0.30	18.13	51.77	1.20
MERIS/OLCI	BRDI+MBR-OC4	0.96	0.98	1.08	1.01	0.31	16.98	49.54	1.18

References

- Antoine, D., Hooker, S. B., Belanger, S., Matsuoka, A., Babin, M., 2013. Apparent optical properties of the Canadian Beaufort Sea – Part 1: Observational overview and water column relationships. *Biogeosciences* 10, 4493–4509. <https://doi.org/10.5194/bg-10-4493-2013>.
- Hu, C., Lee, Z., Franz, B. A., 2012. Chlorophyll *a* algorithms for oligotrophic oceans: A novel approach based on three-band reflectance difference. *J. Geophys. Res.* 117, 1–25.
- Le, C., Zhou, X., Hu, C., Lee, Z., Li, L., Stramski, D., 2018. A color-index-based empirical algorithm for determining particulate organic carbon concentration in the ocean from satellite observations. *J. Geophys. Res. Oceans* 123, 7407–7419.
- Li, L., Stramski, D., Reynolds, R. A., 2016. Effects of inelastic radiative processes on the determination of water-leaving spectral radiance from extrapolation of underwater near-surface measurements. *Appl. Opt.* 55, 7050–7067.
- Morel, A., Gentili, B., Claustre, H., Babin, M., Bricaud, A., Ras, J., Tièche, F., 2007. Optical properties of the “clearest” natural waters. *Limnol. Oceanogr.* 52, 217–229.
- O'Reilly, J. E., Werdell, P. J., 2019. Chlorophyll algorithms for ocean color sensors – OC4, OC5 & OC6. *Remote Sens. Environ.* 229, 32–47.
- Stramski, D., Reynolds, R. A., Babin, M., Kaczmarek, S., Lewis, M. R., Röttgers, R., Sciandra, A., Stramska, M., Twardowski, M. S., Franz, B. A., Claustre, H., 2008. Relationships between the surface concentration of particulate organic carbon and optical properties in the eastern South Pacific and eastern Atlantic Oceans. *Biogeosciences* 5, 171–201.